Published in final edited form as:
Biochim Biophys Acta. 2012 March ; 1820(3): 264–281. doi:10.1016/j.bbagen.2011.09.009.

The Intracellular Trafficking Pathway of Transferrin

Kristine M. Mayle, **Alexander M. Le**, and **Daniel T. Kamei**
Department of Bioengineering, University of California, Los Angeles, CA 90095, United States

Kristine M. Mayle: kristinemayle@ucla.edu; Alexander M. Le: alecle@ucla.edu; Daniel T. Kamei: kamei@seas.ucla.edu

Abstract

Background—Transferrin (Tf) is an iron-binding protein that facilitates iron-uptake in cells. Iron-loaded Tf first binds to the Tf receptor (TfR) and enters the cell through clathrin-mediated endocytosis. Inside the cell, Tf is trafficked to early endosomes, delivers iron, and then is subsequently directed to recycling endosomes to be taken back to the cell surface.

Scope of Review—We aim to review the various methods and techniques that researchers have employed for elucidating the Tf trafficking pathway and the cell-machinery components involved. These experimental methods can be categorized as microscopy, radioactivity, and surface plasmon resonance (SPR).

Major Conclusions—Qualitative experiments, such as total internal reflectance fluorescence (TIRF), electron, laser-scanning confocal, and spinning-disk confocal microscopy, have been utilized to determine the roles of key components in the Tf trafficking pathway. These techniques allow temporal resolution and are useful for imaging Tf endocytosis and recycling, which occur on the order of seconds to minutes. Additionally, radiolabeling and SPR methods, when combined with mathematical modeling, have enabled researchers to estimate quantitative kinetic parameters and equilibrium constants associated with Tf binding and trafficking.

General Significance—Both qualitative and quantitative data can be used to analyze the Tf trafficking pathway. The valuable information that is obtained about the Tf trafficking pathway can then be combined with mathematical models to identify design criteria to improve the ability of Tf to deliver anticancer drugs.

Keywords

transferrin; trafficking; microscopy; radioactivity; SPR; modeling

1. Introduction

Transferrin (Tf) is an iron-binding protein that facilitates iron-uptake in cells. Iron-loaded Tf, also known as holo-Tf, binds to the Tf receptor (TfR) and enters the cell through clathrin-mediated endocytosis [1]. Two types of Tf receptors exist, TfR1 and TfR2 [2]. TfR2 is a close homologue of TfR1 showing 45% identity in the extracellular domain [3]. TfR2 is predominantly found in tissues responsible for regulating iron metabolism such as the liver and small intestine whereas TfR1 distribution is less restricted [4–5]. TfR2 has an

Corresponding author: Daniel T. Kamei Telephone: (310) 206-4826 Fax: (310) 794-5956.

approximately 25-fold reduced holo-Tf affinity compared to TfR1 and is believed to function in overall iron metabolism in addition to cellular iron uptake [6]. In this review, we focus mainly on TfR1 which will be referred to hereafter as simply TfR.

When ligands, such as holo-Tf, are internalized into the cell through clathrin-mediated endocytosis, as shown in Figure 1, endocytosed ligands are sorted along the trafficking pathway into three main populations of endosomes: early endosomes, late endosomes, and recycling endosomes [7]. Studies suggest that ligand sorting begins at the cell surface, separating ligands into two distinct types of early endosomes with different maturation kinetics: dynamic or static [8–9]. Early endosomes maturing quickly into late endosomes comprise the dynamic population, whereas the slower-maturing endosomes comprise the static population. Ligands destined for degradation, such as low-density lipoprotein (LDL), have been shown to be preferentially trafficked to the dynamic population of early endosomes [8]. Tf, on the other hand, follows the recycling pathway and indiscriminately enters both populations of early endosomes [8]. However, since the population of static early endosomes is much greater than that of the dynamic early endosome, Tf becomes enriched in the static population of early endosomes. This pre-early endosomal sorting process is believed to be the first step in the segregation of cargo destined for degradation from those intended to be recycled back to the cell surface.

Both populations of early endosomes undergo a second sorting process to direct cargo intended for recycling to the recycling pathway. This sorting process is initiated with the development of tubular formations in early endosomes, which eventually separate and shuttle cargo either directly back to the cell surface or to the perinuclear endocytic recycling compartment [10]. These two different recycling routes differ in time, since routing through recycling endosomes takes longer than directly being trafficked to the cell surface from the early endosomes [8, 11]. Since Tf is contained within both dynamic and static early endosomes, these tubular formations function to traffic Tf to the recycling pathways from both populations of early endosomes. Ligands intended for degradation remain in the early endosomes, which then mature into late endosomes that subsequently proceed toward the degradation pathway involving lysosomes [12]. An overall diagram of Tf trafficking is shown in Figure 1. For more detailed diagrams of the Tf trafficking pathway, please see reviews by Conner and Schmid [13] and Grant and Donaldson [14], which describe the clathrin-mediated endocytosis and recycling pathways, respectively.

Tf internalization via clathrin-mediated endocytosis and subsequent intracellular trafficking through recycling pathways have been extensively studied. Here, we aim to review the cell-machinery components involved, as well as the methods and techniques that researchers have employed for elucidating the Tf trafficking pathway. These experimental methods can be categorized as microscopy, radioactivity, and surface plasmon resonance (SPR). Microscopy provides a qualitative assessment for determining which cellular machinery-components are involved and the intracellular locations where they function. Radioactivity and SPR, on the other hand, are primarily used in conjunction with mathematical models to determine quantitative information regarding the kinetics of Tf binding, internalization, and recycling. This quantitative information can then be used in mathematical models to identify design criteria for improving the drug delivery efficacy of Tf. Thus, we have structured this review into two main parts. The first part focuses on microscopy experiments that have been performed to elucidate which cellular-components are involved in Tf intracellular trafficking and their locations of action. The second part focuses on radioactivity and SPR experiments, as well as the corresponding mathematical models, which allow us to estimate rate constants for different steps in the intracellular trafficking pathway.

2. Investigating the Tf trafficking pathway using microscopy

2.1. Clathrin-mediated endocytosis

The internalization of Tf into the cell begins with clathrin-mediated endocytosis, where the following core machinery-components are involved: clathrin, adaptor proteins, and dynamin [13, 15–17]. The clathrin complex consists of three heavy and three light chains which form polygonal cages with each other to create curved lattices in the cell membrane that ultimately form clathrin-coated vesicles [18]. In addition to the clathrin complex, adaptor proteins are required for cargo recruitment and for directing clathrin to ligands bound on the surface [19–20]. The final component, dynamin, assembles at the necks of the clathrin-coated invaginations to mediate vesicle formation and scission, where the vesicle separates from the cell membrane [13, 21]. Following endocytosis, the clathrin coat falls off the clathrin-coated vesicle for reuse by the cell [22]. Since Tf is internalized through clathrin-mediated endocytosis, Tf can also be used to study the effects of inhibitors of clathrin-mediated endocytosis. For example, the Kirchhausen research group has used Tf to examine the ability of dynasore, a dynamin inhibitor, to inhibit internalization of ligands through the clathrin-mediated endocytosis pathway [21]. Similarly, Tf has been used to examine the endocytosis inhibitory effects of dynoles, an indole-based dynamin inhibitor, by the McCluskey group [23] and myristyl trimethyl ammonium bromide (MiTMAB), an ammonium salt dynamin inhibitor, by the Robinson group [24].

2.1.1. Clathrin—Initiation of clathrin-mediated endocytosis starts with vesicle budding and formation at clathrin-coated pits on the cell surface. The assembly of multiple clathrin complexes creates a caged geometric structure for producing an invagination in the cell membrane [13]. Clathrin has been extensively studied as a key component in this process. Studies by Kirchhausen and coworkers have indicated the association of clathrin to Tf during endocytosis using spinning disk confocal microscopy [25]. An advantage of confocal microscopy is the imaging of a single plane of interest which eliminates out-of-focus light from other planes [26]. Furthermore, the temporal resolution of spinning disk confocal microscopy allows for live-cell imaging, which is useful in examining the process of clathrin-coated vesicle formation and dissipation, since these processes occur on the order of seconds to minutes [25–26]. In their experiments, the Kirchhausen group incubated red fluorescently-labeled Tf in cells exhibiting green fluorescently-labeled clathrin. Tf was observed to colocalize mostly in the clathrin-coated pits (showing up as yellow) that had just formed within 15 seconds. The association of Tf in newly-formed clathrin-coated pits is consistent with the known clathrin-mediated endocytosis pathway of Tf.

2.1.2. Adaptor protein complex 2 (AP-2)—In one study, the Robinson research group determined that AP-2 is necessary for Tf internalization through using electron microscopy [27]. Thin-section electron microscopy was used to visualize clathrin-coated pits and vesicles identified by the characteristic bristles on the cytosolic side of the vesicles [17]. Figure 2 shows the clathrin-coated pits and vesicles formed during clathrin-mediated endocytosis of Tf. Specifically, TfR antibodies conjugated to gold colloidal particles were used to visualize the clathrin-coated vesicle formation, noted by the collection of gold particles within the clathrin-coated pits and vesicles which are indicated by the black arrowheads. Robinson and coworkers then determined if AP-2 was necessary for Tf internalization by examining how the frequency of clathrin-coated pit formation was affected by AP-2 depletion. Knockdown of AP-2 was accomplished using siRNA against the μ2 subunit of the AP-2 protein complex. Upon doing so, the researchers observed a significant decrease in clathrin-coated vesicles, verifying a role of AP-2 in clathrin-mediated endocytosis of Tf.

Conner and Schmid used fluorescent microscopy to qualitatively examine the uptake of fluorescently-labeled Tf, while AP-2 was inhibited with adaptor-associated kinase 1 (AAK1) [28]. AAK1 is responsible for phosphorylating AP-2, whereby an overexpression of AAK1 causes a decrease in AP-2 function. Using adenoviral-mediated overexpression of AAK1 to inhibit AP-2, Tf uptake was found to be reduced, as noted by its decreased fluorescent intensity within cells, further verifying AP-2 involvement in the clathrin-mediated endocytosis of Tf.

2.1.3. PtdIns(4,5)P_2—Phosphoinositides have also been identified as secondary components mediating vesicle transport [29]. One phosphoinositide, namely phosphatidylinositol (4,5)-bisphosphate, or PtdIns(4,5)P_2, plays an essential role in regulating clathrin-mediated endocytosis [19, 29–34]. Specifically, PtdIns(4,5)P_2 interacts and binds with the α and μ2 subunit of AP-2, an adaptor protein complex responsible for recruiting clathrin to sites of bound ligands [34–35]. A study by De Camilli and coworkers [30] examined the effects of Tf uptake after inactivating PtdIns(4,5)P_2 with a recently developed rapamycin-induced heteroligomerization strategy [36]. This method, which is able to quickly deactivate PtdIns(4,5)P_2, employs a phosphatase, namely Inp54p, to dephosphorylate PtdIns(4,5)P_2. However, Inp54p is mainly present in the cytosol whereas clathrin formation occurs at the surface. To overcome this, Inp54p needs to be brought to the cell surface. This was accomplished by conjugating Inp54p to FKBP, a protein, which when under the presence of rapamycin, will crosslink to mTOR, a plasma membrane-localized protein. Thus, the addition of rapamycin to cells brings Inp54p-FKBP conjugates, initially localized in the cytosol, to the cell surface within close enough proximity to dephosphorylate and inactivate PtdIns(4,5)P_2 where clathrin-coated pit formation occurs. Using spinning-disk confocal microscopy, a reduction of internalized fluorescently-labeled Tf was observed when iRAP, an analogue of rapamycin, was added. Furthermore, inactivation of PtdIns(4,5)P_2 via rapamycin also eliminated the presence of clathrin in clathrin-coated pits as determined by total internal reflectance fluorescence (TIRF) microscopy, which is described below. These results confirm the role of PtdIns(4,5)P_2 as one of the machinery components involved in the regulation of clathrin-mediated endocytosis of Tf.

TIRF microscopy is a visualization method that can be used to capture events near the plasma cell membrane [37]. Its use for imaging clathrin dependent endocytosis was developed by the Almers research group [38]. This method uses total internal reflection at a solid/liquid interface to create an electromagnetic wave that exponentially decays in the liquid containing the sample. Due to the exponential decay of the wave, it results in only exciting fluorophores within 100 – 200 nm of the cell membrane without exciting regions deeper in the cell. This in turn leads to images with low background and less out-of-focus fluorescence [37]. The temporal and three-dimensional resolution capabilities of this method allows for real-time imaging of vesicle formation and movement within the cell [39].

Additional studies performed by the Meyer research group have also verified PtdIns(4,5)P_2 as responsible for mediating AP-2 recognition and recruitment of surface bound ligands [33]. As in the previous studies, PtdIns(4,5)P_2 was reduced by the rapamycin-induced heteroligomerization method. Using laser-scanning confocal microscopy, PtdIns(4,5)P_2 inactivation was shown to result in decreased Tf internalization as shown in Figure 3. Furthermore, PtdIns(4,5)P_2 inactivation increased the levels of TfR at the surface, as visualized through using immunofluorescence, or fluorescent antibodies against TfR. To visualize the effect of PtdIns(4,5)P_2 inactivation on AP-2 association at the cell surface, AP-2 immunofluorescence in conjunction with TIRF microscopy were used to visualize clusters of AP-2 at the cell surface. The results showed that when PtdIns(4,5)P_2 is inactivated, AP-2 is diffuse over the cell surface. However, in control cells with normal

PtdIns(4,5)P_2 activity, AP-2 clusters were distinct at segregated locations in the plasma membrane. PtdIns(4,5)P_2 inactivation also led to loss of cell surface clustering of fluorescently-labeled Tf, as visualized with scanning-laser confocal microscopy. In another experiment using TIRF imaging of fluorescently-labeled clathrin, PtdIns(4,5)P_2 inactivation was shown to have minimal effect on clathrin assembly. Together, these results suggest that PtdIns(4,5)P_2 is a primary regulator of AP-2 and not directly of clathrin assembly itself.

2.1.4. Dynamin 2, cortactin, and src kinase—When Tf binds TfR on the cell surface, it activates a cascade believed to mediate its specific endocytosis into the cell [39–40]. This endocytosis cascade has been shown by McNiven and coworkers to require src kinase, dynamin 2 GTPase, and the actin-binding protein, cortactin, [39]. Dynamin 2 and cortactin together are activated by the src kinase to regulate the actin dynamics that control vesicle formation upon ligand binding [41]. The McNiven research group used TIRF microscopy to visualize dynamin 2 and cortactin dynamics during clathrin-mediated endocytosis of Tf. Their results showed that dynamin 2 levels increased significantly upon the addition of Tf. Dynamin 2 was found to form rings at the cell surface where vesicles eventually formed. Furthermore, cortactin was observed to associate with dynamin 2 just prior to vesicle scission. This coincided with an observed depletion of TfR at the cell surface which confirms that Tf was being internalized concurrently with vesicle formation.

Using immunoprecipitation against TfR, followed by Western blot analysis, the McNiven group observed association of cortactin and dynamin 2 to TfR in cells cultured with Tf. This suggests that the binding of Tf to the cell surface may induce recruitment of endocytic machinery involving dynamin 2 and cortactin at its binding site. To determine whether dynamin 2 and cortactin were being activated during Tf internalization, ^{32}P was used to label all cell proteins. Upon lysing the cells, collecting the proteins via immunoprecipitation, and separating the proteins by SDS-PAGE, subsequent autoradiography results showed increased phosphorylation levels of dynamin 2 and cortactin, as indicated by their increased band intensity, in cells exposed to Tf. To determine whether src kinase is responsible for activation of dynamin 2 and cortactin, McNiven and coworkers added increased levels of src kinase to dynamin 2 and cortactin purified from *Escherichia coli*. As expected, they observed an increase in band intensity of phosphorylated dynamin 2 and cortactin, suggesting that src kinase was responsible for activation. Furthermore, these endocytic machinery proteins have been known to be phosphorylated on tyrosine residues [42]. Defective forms of dynamin 2 and cortactin, mutated at the tyrosine phosphorylation sites, also showed minimal phosphorylation. These results suggest that src kinase is likely responsible for activating dynamin 2 and cortactin.

2.2. Early and late endosomes

As mentioned earlier, after clathrin-mediated endocytosis into the cell which is regulated by AP-2, PtdIns(4,5)P_2, dynamin2, cortactin, and src kinase, Tf indiscriminately enters into two populations of early endosomes that exhibit either fast or slow maturation kinetics. Specifically, the dynamic population of early endosomes matures faster than their static population counterparts [8]. The sorting process for directing cargo to either of these populations is believed to begin at the cell surface [9]. Since Tf is trafficked through early endosomes, it can be used as a tool to stain early endosomes and subsequently help reveal whether ligands of interest are traveling through this pathway as well. For example, the trafficking pathway of viruses, such as the human adenovirus, through the early endosome has been examined using this method [43]. Tf has also been used to determine whether proteins internalized via clathrin-independent endocytosis come in contact with early endosomes that contain cargo from clathrin-dependent endocytosis [44].

2.2.1. Dynamic and static populations of early endosomes—Zhuang and coworkers identified the static and dynamic populations of early endosomes using real-time live-cell fluorescent imaging and Rab GTPase markers of the early and late endosomes [8]. Rab GTPases are specifically associated with different organelles within the cell. For example, Rab5 and Rab7 are mainly present in early and late endosomes, respectively [45]. In their experiments, the researchers used fluorescently-labeled Rab5 to stain early endosomes, while fluorescently-labeled Rab7 was used to stain the late endosomes. Real-time imaging allowed the researchers to visualize the development of the early and late endosomes with temporal resolution. Their results suggested the presence of two distinguishable populations of early endosomes: dynamic and static. This was due to the fact that only a low fraction of Rab5-positive, or early, endosomes were observed to mature rapidly into late endosomes as noted through their acquisition of Rab7, a late endosome marker, within approximately 30 seconds of formation. These rapidly maturing endosomes comprise the dynamic group of early endosomes. Conversely, the majority of the early endosome population does not acquire Rab7 within 100 seconds and comprise the static, slower maturing, group of early endosomes.

2.2.2. Tf is indiscriminately trafficked to both dynamic and static early endosomes—Zhuang and coworkers also examined the trafficking of LDL and Tf, which are known to follow degradation and recycling pathways, respectively [8]. Again using real-time fluorescent imaging of live cells, the researchers were able to show that a majority of LDL was trafficked to dynamic endosomes containing both Rab5 and Rab7 soon after clathrin-mediated endocytosis. This suggests that cargo destined for degradation, such as LDL, will be preferentially trafficked to dynamic early endosomes. On the other hand, Tf showed no preference and was sorted into both static (Rab5-associated) and dynamic (Rab5 and Rab7-associated) populations. Nonetheless, since the population of static early endosomes is much greater than the population of dynamic early endosomes, Tf naturally becomes enriched in the static early endosome population.

2.2.3. Pre-early endosomal sorting occurs at the cell surface—It is hypothesized that the sorting of cargo into different endosomal compartments begins at the cell surface [9]. Studies by Corvera and coworkers indicate that segregation of Tf at the plasma membrane occurs immediately after binding and is likely the cell's initial cargo sorting mechanism [9]. In their experiments, TIRF microscopy was utilized due to the method's temporal resolution and its high sensitivity to fluorophores within 100 – 200 nm of the cell surface. Fluorescent epidermal growth factor (EGF) and Tf were incubated in cells as they are known to follow the degradation and recycling pathways, respectively. Within 60 seconds of addition, both EGF and Tf had bound to the cell surface and had already separated into distinct groups while exhibiting minimal colocalization with each other. Figure 4 shows a TIRF microscopy image of Tf (green) and EGF (red) within 60 seconds of addition to the cell. Both EGF and Tf separate into distinct groups while exhibiting minimal colocalization. The researchers hypothesize that this separation of ligands may be due to segregated regions of receptors in the plasma membrane. Nonetheless, the mechanism by which ligand sorting at the cell surface eventually leads to two different populations of dynamic and early endosomes is unclear. Two possible mechanisms are suggested by the Corvera research group: (i) internalization of segregated ligand clusters occurs directly into distinct vesicle compartments, or (ii) ligand clusters migrate to clathrin-coated pits before being internalized into dynamic or static early endosomal compartments. Additional experiments to elucidate and confirm the mechanism of ligand sorting at the surface to the different populations of early endosomes remains to be resolved.

The pre-early endosomal sorting process at the cell surface has also been shown to rely on adaptor proteins which are an important constituent of vesicles and believed to be involved

in cargo recruitment. The Zhuang research group investigated the role of AP-2 in producing early or late endosomes [8]. Similar to before, static early endosomes were distinguished by their continued association with Rab5, an early endosome marker. Conversely, dynamic early endosomes exhibiting quicker maturation kinetics were identified through co-association of Rab5 and Rab7, a late endosome marker. Using siRNA against the μ2 subunit of AP-2, they found that it subsequently caused a significant decrease in the static (Rab5 associated) early endosome population while not affecting dynamic (Rab5 and Rab7 co-associated) early endosomes. In other words, AP-2 depletion caused the fractional population of dynamic early endosomes to increase, while that of static early endosomes decreased. Since a knockdown of AP-2 leads to a decrease in the formation of static early endosomes, but not dynamic early endosomes, it suggests that the AP-2 adaptor protein complex likely plays a role in allowing the entry of cargo destined for the static early endosome population. On the other hand, since dynamic early endosomes remain unaffected by AP-2 knockdown, endocytosis into this population is likely independent of the AP-2 protein complex.

Studies also indicate that ligand sorting into the distinct groups of early endosomes is dependent on microtubule engagement. Zhuang and coworkers observed that endocytosed cargo destined for dynamic early endosomes typically engage microtubules on a much larger scale than cargo destined for the static early endosome population. Using real-time fluorescent imaging of live cells, dynamic early endosome populations were shown to be highly mobile, while a disruption of microtubules prevented selective sorting to the different early endosomes [8]. To prevent microtubule formation, nocodazole, an agent that interferes with microtubule polymerization was used. LDL and influenza, which mostly join dynamic early endosomes, were found to lose their selective sorting into dynamic early endosomes upon microtubule inhibition. Tf, which did not have selective sorting into the different early endosome compartments to begin with, was still directed to their original endosomal locations under microtubule inhibition. The researchers hypothesize that newly endocytosed vesicles would need to be able to rapidly engage microtubules in order to encounter and fuse with the dynamic early endosomes that are also mainly moving on these microtubules themselves. The researchers infer that microtubule engagement is necessary for ligand sorting between dynamic and early endosomes.

2.3. Tf Recycling

Once in the early endosome, cargo is sorted to their corresponding degradation or recycling pathways. Cargo intended for recycling can return back to the cell surface through either a fast route of being directly transported back to the plasma membrane, or alternatively, through a slower route of being trafficked first to recycling endosomes before returning to the surface [14, 46]. Cargo intended for degradation remain in the early endosomes as they mature into late endosomes, which eventually lead to the degradation pathway. The recycling from early endosomes is controlled by various GTPases and their regulators, as well as actin regulators [14]. Due to its pathway through recycling endosomes, Tf can be used as a tool to elucidate the trafficking pathways of other ligands that proceed through recycling pathways, such as the E-cadherin protein, anthrax toxin receptor 1, and mouse polyomavirus [47–49].

2.3.1. Early endosomal sorting of Tf to recycling pathways—The recycling of Tf to the cell membrane from both dynamic and static early endosomes has been observed by the Zhuang research group, where tubular formations, containing cargo destined for recycling, develop and eventually separate [8]. As previously mentioned, static and dynamic early endosomes were distinguished by Rab5 association and Rab5/Rab7 coassociation, respectively. Real-time fluorescent imaging revealed that Tf moves into tubular formations

in both the static and dynamic early endosomes before separating. These vesicles then deliver Tf to the perinuclear recycling compartment or directly to the plasma membrane [46]. Recycling endosomes were identified with fluorescently labeled Rab11, a GTPase marker within recycling compartments that is responsible for regulating Tf trafficking from recycling endosomes [50–51]. Results showed Rab11 colocalized with fluorescently labeled Tf, verifying that Tf was indeed delivered to the endocytic recycling compartment from early endosomes.

2.3.2. GTPase regulators mediating Tf recycling—Rab4, a GTPase localized primarily in early endosomes, has also been determined to mediate the Tf trafficking pathway [52]. Mellman and coworkers showed that Tf became increasingly trafficked to the recycling vesicles when Rab4 was overexpressed [53]. Using electron microscopy, which provides visualization of the cell and its vesicular and plasma membrane structures, the researchers observed that an overexpression of Rab4 caused the majority of Tf to be localized within tubular structures and vesicles headed towards the recycling compartment or cell surface. Compared to control cells, these cells overexpressing Rab4 also exhibited decreased amounts of Tf localized in early endosomes, which were identified by their smaller diameters. These results indicate that Rab4 is involved in trafficking Tf to recycling vesicles from early endosomes through tubular formations. However, in another study by the van der Sluijs research group, RNAi against Rab4 resulted in increased Tf recycling [54]. In this experiment, the researchers used fluorescence microscopy to visualize fluorescent Tf internalized within cells. In cells with RNAi against Rab4, less Tf was found to remain internalized, suggesting that increased amounts of Tf were exiting the cells compared to control cells. Thus, it is still not certain what function Rab4 serves in Tf recycling, and this point has also been noted in other reviews [14].

Sabatini and coworkers have shown that the Rab11 GTPase is required for Tf trafficking to the cell surface from the endocytic recycling compartment but not from early endosomes [55]. In normal cells, fluorescent Tf was observed to be dispersed in vesicles throughout the cytoplasm in addition to being concentrated near the juxtanuclear region, which corresponds to the recycling compartment of the slow recycling pathway. In cells expressing the dominant negative Rab11 mutant, Tf no longer associated with the juxtanuclear region and remained in vesicles within the cytoplasm. Thus, this indicates that Rab11 is responsible for directing Tf through the slow recycling pathway through the endocytic recycling compartment.

DAKAP2 has been shown to regulate Tf trafficking to recycling endosomes likely through interactions with Rab4 and Rab11 by Taylor and coworkers [51]. A reduction in Tf association within the juxtanuclear compartment was visualized using immunofluorescent microscopy when DAKAP2 was knocked down, whereas in normal control cells, more Tf association in the juxtanuclear compartment was observed. This compartment near the nucleus corresponds to the recycling compartment of the slow recycling pathway. Furthermore, DAKAP2 was shown to bind to Rab4 and Rab11, and while it is unclear how this interaction affects recycling, the researchers hypothesize that DAKAP2 may be involved in recruiting Rab11 to membranes containing Rab4.

There is also evidence for another GTPase, Rab35, to play a role in Tf recycling through the fast recycling pathway. In a study by the Echard group, the researchers used fluorescence-activated cell sorting (FACS) to quantitatively measure the amount of fluorescently-labeled internalized Tf at various time points [56]. By measuring the internalized Tf over time as a fraction of the initial internalized Tf, the researchers could determine the amount of Tf being recycled to the surface. In cells expressing Rab35 S22N, a dominant negative mutant, significantly less Tf was trafficked to the cell surface after 5 min of Tf addition compared to

control cells. However, after 15 minutes, Tf recycling was similar between control cells and Rab35 S22N expressing cells. This suggests that Rab35 regulates the fast recycling pathway of Tf. However, in another study by the McPherson and Ritter group, their results indicate that a Rab35 knockdown had no significant effect on Tf recycling as quantified through FACS flow cytometry [57]. Whether or not Rab35 is involved in Tf recycling from early endosomes still remains to be resolved.

Peränen and coworkers provided evidence that Rab8 GTPase activity is involved in transporting Tf to the pericentriolar region through the slow recycling pathway [58]. In their experiments, cells were depleted of Rab8 with siRNA. Using time-lapse fluorescence microscopy, the researchers found that once internalized, Tf remained scattered throughout the cytoplasm in Rab8-depleted cells, whereas control cells showed a presence of Tf in the cytoplasm in addition to the perinuclear endocytic recycling compartment. This led the researchers to hypothesize that Rab8 may control Tf recycling traffic from early endosomes to the recycling compartment. Nonetheless, it was found that Tf recycling to the cell surface still occurred despite Rab8 depletion. It is likely that recycling still continues through the fast recycling pathway from early endosomes directly to the plasma membrane, bypassing the pathway to the endocytic recycling compartment controlled by Rab8. In another study, Henry and Sheff reported findings suggesting that Rab8 directs cell-synthesized cargo from the trans-Golgi network to recycling endosomes, but is not responsible for directing endocytosed cargo from early endosomes to recycling endosomes [59]. Since Tf recycling would occur from early endosomes (not the trans-Golgi network) to recycling endosomes, the studies of Henry and Sheff suggest that Rab8 may not be directly involved in Tf recycling.

The Rab22a GTPase has been shown to regulate Tf trafficking from early endosomes to recycling endosomes by the Mayorga research group [60]. Confocal microscopy images revealed that fluorescently-labeled Tf was retained in siRNA Rab22a-depleted cells after one hour. Conversely, most of the Tf had recycled and exited in control cells after one hour. Furthermore, Rab22 depleted cells seemed to lack a perinuclear recycling compartment, thus causing Tf to mainly associate at the cell periphery. Control cells, on the other hand, showed Tf accumulation dispersed throughout the cytoplasm as well as the perinuclear recycling compartment region. Additional experiments in Rab22a-depleted cells showed colocalization between an early endosome marker, namely EEA1, and Tf thereby suggesting that Tf was being retained within early endosomes. This indicates that Rab22a allows Tf trafficking from early endosomes to recycling endosomes.

ADP-ribosylation factor (Arf6) is a GTPase that regulates Tf recycling by controlling actin remodeling [61–62]. In a study by Montagnac, Chavrier, and coworkers using TIRF microscopy, Tf recycling was shown to be dependent on Arf6 [63]. In control cells, fluorescent Tf was observed to exit the cell quickly. However, in cells expressing the dominant-negative mutant $Arf6^{T27N}$, Tf did not as readily exit the cell, suggesting an impairment in Tf recycling. Since this decrease in Tf recycling only occurred when the recycling time was less than 8 minutes, the researchers believe that Arf6 may be responsible for mediating Tf in the fast recycling pathway.

Studies have indicated that some GTPase regulators of Tf recycling, such as Rab22a, may affect Tf recycling pathways in a different manner depending on the specific cell-type. Donaldson and coworkers have reported that an inhibition of Rab22a does not completely inhibit Tf recycling in HeLa cells since it is hypothesized that the endosomal recycling compartment in HeLa cells is a multidomain compartment with multiple recycling routes from the endosomal recycling compartment [64]. Conversely, in Chinese hamster ovary cells, Tf recycling is believed to follow a singular endosomal recycling pathway which is

mediated by Rab22a [64]. Furthermore, there are also many additional Rab and Arf GTPase regulators and effectors that work in conjunction to control Tf recycling. These regulators and effectors which include Rab11FIP2, Rab11FIP3, Rab11FIP5, Rabenosyn5, SEC10, JIP3, JIP4, ASAP1, ACAP1, and RME-4 have been reviewed by Grant and Donaldson [14].

2.3.3. Actin regulators mediating Tf recycling—The receptor mediated endocytosis/Eps15 homology domain (RME-1/EHD) family of proteins is believed to mediate cargo trafficking to the plasma membrane from recycling compartments [65]. In mammals, four EHD paralogs exist: EHD1, EHD2, EHD3, and EHD4. In *Caenorhabditis elegans* (*C. elegans*) the EHD family protein, RME-1, has approximately 67% identity with the mammalian EHD1 and has been tested in various studies to determine its role in endocytosis and recycling [66]. Horowitz and coworkers examined Tf recycling in EHD1-deficient mouse embryonic fibroblasts grown *in vitro* [67]. Laser scanning confocal microscopy images revealed rapid Tf clearance from wild-type cells within 60 minutes. However, in EHD1-deficient cells, Tf clearance from cells was not as rapid, while there was a marked accumulation of Tf within recycling endosomes located near the cell nucleus. This suggests that Tf is likely remaining in the perinuclear endocytic recycling compartment, which is part of the slow recycling pathway. These results suggest that EHD1 is one of the machinery components responsible for controlling Tf recycling from the endosomal recycling compartment. EHD1 regulation of Tf recycling may possibly be a result of controlling actin dynamics as studies have shown RME-1/EHD colocalization with actin regulators, such as Arf6, in the tubular formations of endosomes [68].

Grant and coworkers have shown in *C. elegans* that AMPH-1, a member of the amphiphysin/BIN1 protein family in mammals, works together with RME-1/EHD to regulate Tf trafficking from recycling compartments to the plasma membrane [69]. They observed through confocal microscopy images that AMPH-1 colocalizes with RME-1 in recycling endosomes stained with fluorescent SDPN-1, a known marker of recycling endosomes in *C. elegans*. Additionally, AMPH-1 defective mutants illustrated unusual recycling endosome morphology as well as Tf recycling inhibition. In HeLa cells, a depletion of amphiphysin 2, alternatively known as BIN1, led to a disruption of recycling compartment tubules visualized by immunostained EHD1. These results suggest that the amphiphysin/BIN1 protein family is involved in regulating Tf recycling.

Sorting-nexin 4 (SNX4) has been shown by the Cullen research group to mediate Tf trafficking into the recycling compartment [70]. Quantitative analysis using radiolabeled Tf showed decreased levels of Tf in siRNA SNX4-depleted cells. Similarly, qualitative analysis using Western blotting revealed that TfR levels were also significantly reduced in siRNA SNX4-depleted cells as well. Lysosomal inhibitors were used in conjunction with SNX4-depletion to test whether the reduction of TfR was due to lysosomal degradation. In fact, lysosomal inhibitors restored TfR levels, consequently implicating that TfR was being degraded in the lysosomal pathway as a result of SNX4 suppression. Since a depletion of SNX4 leads to degradation of TfR, this is likely due to a missorting of TfR due to blocking entry to the recycling pathway from the early endosome, thus diverging TfR towards the degradation pathway. Cullen and coworkers hypothesize that SNX4 is responsible for directing Tf away from the early endosome to recycling pathways. The researchers also show that SNX4 binds to KIBRA, a dynein-binding protein, and may regulate dynein function. Dynein is a microtubule motor protein responsible for membrane tubulation. Thus, Cullen and coworkers propose that SNX4 mediates transport of Tf to recycling endosomes through driving membrane tubulation to traffic Tf out of early endosomes.

3. Obtaining a quantitative understanding of Tf trafficking using radioactivity, surface plasmon resonance, and mathematical models

Radiolabeling techniques have been used to evaluate binding specificity and saturation [71–73], the effects of temperature [71, 74–75] and concentration [71, 76–77] on internalization, cellular localization [78–80], exocytosis of Tf through pulse-chase studies [75, 81], and release of intact Tf [71, 75, 82–84]. Additionally, chemical inhibitors have been used to help elucidate the Tf trafficking pathway by monitoring changes in trafficking of radiolabeled Tf through the cell [71, 73, 85–88]. This section of the review, however, will focus on radiolabeling techniques, which when combined with mathematical models of the Tf trafficking pathway, can be used to determine equilibrium binding constants, rate constants, cycle times, and the activation energy in the internalization rate constant. Furthermore, surface plasmon resonance will be discussed, since it can be used to quantitatively measure association and dissociation rate constants, and therefore, equilibrium dissociation constants.

3.1. Binding at the Cell Surface

3.1.1. Scatchard Analysis—The Scatchard analysis, in conjunction with radiolabeling, has been used to evaluate the equilibrium binding affinity between a ligand and its receptor. This technique has been used extensively as a method to determine the equilibrium dissociation constant, K_D, and the total number of receptors present at the cell surface, $R_{s,T}$. The equilibrium dissociation constant can be defined as follows:

$$K_D \equiv \frac{L_{eq} R_{s,eq}}{C_{s,eq}} \tag{1}$$

where L_{eq} is the free Tf ligand concentration at equilibrium, $R_{s,eq}$ is the number of free Tf receptors at the cell surface at equilibrium, and $C_{s,eq}$ is the number of cell-surface Tf/TfR complexes at equilibrium. The use of low temperatures and/or energy inhibitors minimized trafficking and receptor synthesis in these experiments. Therefore, the total number of cell-surface receptors ($R_{s,T}$) remains constant, and equal to $R_{s,eq}$ plus $C_{s,eq}$. Using this equality for $R_{s,T}$, $R_{s,eq}$ in Eq. (1) can be replaced in terms of $R_{s,T}$ and $C_{s,eq}$ resulting in the following equation:

$$\frac{C_{s,eq}}{L_{eq}} = -\frac{1}{K_D} C_{s,eq} + \frac{R_{s,T}}{K_D} \tag{2}$$

In the Scatchard plot shown in Figure 5, $C_{s,eq}$, denoted as *Bound*, is determined by measuring the bound radiolabeled ligand at equilibrium. On the other hand, L_{eq}, represented by *Free*, is found by measuring the concentration of free ligand present in the medium at equilibrium. Linear regression of bound ligand/free ligand (*Bound/Free* or $C_{s,eq}/L_{eq}$) as a function the amount of bound ligand (*Bound* or $C_{s,eq}$) at equilibrium yields a slope equal to negative of the inverse of K_D. The total number of receptors per cell ($R_{s,T}$) can then be calculated from the y-intercept, since it is equal to $R_{s,T}/K_D$.

In one study, Kohno and Tokunaga were able to estimate the total number of receptors per cell as 9.24×10^4 with an apparent K_D of 1.3 nM for reticulocyte cells, using low temperatures to inhibit trafficking [73]. Similar analyses have been performed using low temperatures as a means to inhibit trafficking [71–72, 75, 89]. However, it should be noted that, even at 4°C, some Tf will enter the cell, albeit at a much slower rate, and a 1 hour incubation may not be sufficient to reach binding equilibrium in this system. Another option, if using a physiological temperature, is to block internalization with energy inhibitors, such

as sodium azide. Using this method, Eckelman and coworkers found the K_D and total number of receptors per cell to be 9.2 ± 9.6 nM and 0.9 ± 0.5 × 10^5 #/cell, respectively [82]. In general, these studies demonstrated that proliferating cell types express large numbers of Tf receptors, which bind with high affinity, or low K_D values, to Tf.

3.1.2. Surface Plasmon Resonance—Another technique, surface plasmon resonance (SPR), can also be used to quantify the equilibrium parameter of Tf binding to TfR, as well as the corresponding rate constants for Tf binding and unbinding from TfR. In these experiments, TfR is bound to the SPR sensor surface, and the interaction between the ligand and receptor can be detected as a change in refractive index [90]. As Tf binds the receptor, the buildup of protein causes an increase in the refractive index. Thereby, through using SPR, Tf binding can be observed and analyzed in real-time.

Two methods have been applied to find the equilibrium dissociation constant for Tf binding to TfR from SPR data. The first method fits experimental data to a form of the Hill equation to determine the equilibrium dissociation constant. This form of the Hill equation comes from equating the fraction of occupied binding sites as the number of Tf/TfR complexes divided by the total number of available binding sites:

$$\frac{B_{eq}}{B_{max}} = \frac{C_{eq}}{C_{eq}+R_{eq}} \tag{3}$$

where C_{eq} is the number of Tf/TfR complexes at equilibrium, R_{eq} is the number of free TfR at equilibrium, B_{eq} is the equilibrium binding response, and B_{max} is the maximum binding response measured experimentally when an excess of ligand is used. Equation (3) can be rewritten in terms of the injected ligand concentration, *[L]*, by solving Eq. (1) for C_{eq} and replacing the ligand concentration at equilibrium, L_{eq}, by *[L]*. This substitution is valid, since experimentally, the injected ligand is allowed to flow over the receptors until the association rate equals the dissociation rate, resulting in a constant response and no further change in the overall injected ligand concentration [91]. After this substitution and additional simplification, Eq. (3) becomes:

$$\frac{B_{eq}}{B_{max}} = \frac{[L]}{[L]+K_D} \tag{4}$$

The equation above is a form of the Hill equation that assumes a 1 ligand binding to 1 receptor model, in which there is a single class of noninteracting sites exhibiting noncooperativity. Nonlinear regression analysis of B_{eq} versus the logarithm of [L] can then be used to determine the K_D values.

In the case of holo-Tf binding to TfR, Bjorkman and coworkers first used gel-filtration chromatography to determine the binding stoichiometry, and their results suggested that TfR dimerizes such that two holo-Tf bind to every two Tf receptors. As a result, Bjorkman and coworkers used a binding model that considers two classes of non-interacting binding sites on a TfR homodimer with two different K_D values; therefore, the data was fit using a heterogeneous 2:2 model. Since these binding events are considered to be independent, B_{eq} can be represented by the sum of the individual binding responses at equilibrium (such as the one in Eq. (4)), taking into consideration the fraction of total binding sites in each class, f_1 and f_2:

$$\frac{B_{eq}}{B_{max}} = f_1\left[\frac{[L]}{[L]+K_{D,1}}\right] + f_2\left[\frac{[L]}{[L]+K_{D,2}}\right] \quad (5)$$

where $f_1 + f_2 = 1$ [92]. Experimentally, Bjorkman and coworkers applied long injection time periods with slow flow rates over biosensor chips with high densities of TfR covalently bound to the chips, and allowed binding to reach equilibrium [93]. Subsequently, plotting B_{eq} as a function of injected ligand concentration and fitting this experimental data to the model in Eq. (5), the equilibrium binding dissociation constants, $K_{D,1}$ and $K_{D,2}$, were found to be 1.9 nM and 29 nM, respectively, where f_1 and f_2 were 0.51 and 0.49, respectively.

A second method used to calculate the equilibrium binding constant from SPR data uses the association and dissociation rate constants, k_a and k_d. Bjorkman and coworkers used a flow rate of 50 μL/min and performed 4 minute binding and dissociation experiments at a variety of Tf concentrations [94]. For the binding experiments, a solution containing Tf is injected over the immobilized TfR and binding is measured as a function of time. The dissociation experiment then follows, in which buffer containing no Tf is injected and the dissociation of Tf from TfR is recorded. The kinetic constants are then calculated using CLAMP 99, a global data analysis program that combines numerical integration and nonlinear curve fitting techniques to simultaneously analyze the association and dissociation data [95]. The program starts by generating a series of differential equations based on the chosen reaction model using arbitrarily chosen rate constants. Subsequently, using numerical integration, differential equations are generated to simulate data which are subsequently subtracted from the experimental data to calculate the χ^2 value. The program then adjusts the rate constants to minimize the χ^2 value. This process is repeated until the χ^2 value is less than 0.1%. In this case, the Bjorkman research group chose a 2:1 bivalent ligand reaction model, where two Tf bind sequentially to a single TfR homodimer. In the proposed model, one molecule of Tf reversibly binds to the first binding site on the TfR homodimer, TfR_{hd}, before a second molecule of Tf reversibly binds to the second site:

$$Tf + TfR_{hd} \underset{k_{d1}}{\overset{k_{a1}}{\rightleftarrows}} Tf - TfR_{hd} \quad (6)$$

$$Tf + Tf - TfR_{hd} \underset{k_{d2}}{\overset{k_{a2}}{\rightleftarrows}} Tf - TfR_{hd} - Tf \quad (7)$$

where k_{a1} and k_{a2}, and k_{d1} and k_{d2} represent the association and dissociation rate constants for reactions 1 and 2, respectively. The equilibrium dissociation constant for each reaction can then be calculated using the following equation:

$$K_{D,i} = \frac{k_{d,i}}{k_{a,i}} \quad (8)$$

where i designates the reaction number. Using Eq. (8), Bjorkman and coworkers found the equilibrium dissociation constants for reactions 1 and reaction 2, $K_{D,1}$ and $K_{D,2}$, to be 1.1 nM and 29 nM, respectively [94].

3.1.3. Combining radioactivity and mathematical modeling to estimate association and dissociation rate constants—The kinetic parameters of holo-Tf/TfR binding and dissociation at the cell surface can be determined by combining radioactivity experiments with mathematical modeling. In order to describe the rate of binding of holo-Tf to TfR on the cell surface, Lodish and coworkers derived a mathematical

model, which expanded upon previously described models for the epidermal growth factor and asialoglycoprotein receptors [96–97]. Figure 6 depicts the kinetic parameters of the Tf trafficking pathway.

The following assumptions were used in the model derivation: (i) All functional receptors behave identically. (ii) There is no appreciable degradation or synthesis of receptors during short periods of time. (iii) The total number of receptors is constant [98].

Performing a species balance on the number of free receptors at the cell surface, R_s, yields the following equation:

$$\frac{dR_s}{dt} = k_d C_{s,holo} - k_a L R_s \tag{9}$$

where k_d is the dissociation rate constant of the holo-Tf/TfR complex at the cell surface ($C_{s,holo}$), and k_a is the association rate constant of holo-Tf (L) to TfR (R_s) at the cell surface.

Using energy inhibitors and excess radiolabeled Tf to prevent internalization and the formation of free receptors, respectively, Eq. (9) can be simplified. However, it should be noted that although it was assumed that Tf does not dissociate to form free receptors, it is expected that some unbinding will occur. Nevertheless, eliminating the appropriate terms, the following equation was obtained.

$$\frac{dR_s}{dt} = - k_a L R_s \tag{10}$$

Assuming that the ligand concentration, L, is constant over the time course of the experiment, since the holo-Tf concentration in the medium was in excess and was not expected to significantly change throughout the experiment, Eq. (10) was integrated and rearranged; applying the initial condition, where the free receptors present on the cell surface at $t = 0$ is $R_{s,0}$.

$$\ln\left(\frac{R_s}{R_{s,0}}\right) = - k_a L t \tag{11}$$

The half-time ($t = t_{1/2}$) of association can be determined from Eq. (11) using R_s equal to $½R_{s,0}$ at the half-time.

$$t_{1/2} = \frac{\ln(2)}{k_a L} \tag{12}$$

By measuring the cell associated radioactivity, the number of cell-surface complexes can be determined, and the fraction of free receptors can be expressed with the following equation:

$$\frac{R_s}{R_{s,0}} = \frac{R_{s,0} - C_{s,holo}}{R_{s,0}} = 1 - \frac{C_{s,holo}}{C_{max}} \tag{13}$$

where the number of free receptors at time t, R_s, is equal to the initial number of free receptors, $R_{s,0}$, minus the number of receptors bound to Tf at any time, t, $C_{s,holo}$. Finally, $R_{s,0}$ can be replaced by C_{max}, which is the maximum amount of Tf that binds to the cell, since all cell-surface receptors were assumed to be bound to Tf due to the addition of excess

Tf. Therefore, by substituting Eq. (13) into Eq. (11), the half-time of association can be determined from a semi-logarithmic plot of the fraction of free receptors, expressed as $[1-(C_{s,holo}/C_{max})]$, as a function of time (Figure 7). Equation (12) can then be used to estimate the product of the association rate constant and the ligand concentration, k_aL.

Using this approach, Lodish and coworkers found the k_aL value to be 0.23 min^{-1} at physiological temperature. When this value is divided by the ligand concentration, which is expected to be relatively constant at 77 nM throughout the experiment, k_a is estimated to be 2.99×10^6 min^{-1} M^{-1} [98]. Czech and coworkers also used this approach, and found the association rate constant to be 2.7×10^7 min^{-1} M^{-1} [99]. Using a comparable model, Sainte-Marie and coworkers found the rate constant for association of Tf to TfR, k_a, to be $(1.2 \pm 0.2) \times 10^6$ min^{-1} M^{-1} [100]. In a similar manner, Glass and coworkers found k_a to be 1.2×10^7 min^{-1} M^{-1} [101]. Table 1 shows the rate constants that have been estimated for each step of the Tf trafficking pathway.

Similarly, Lodish and coworkers determined the rate constant for dissociation of holo-Tf from TfR at the cell surface using the half-time for dissociation [98]. The rate of change of the receptors bound to Tf at the cell surface can be derived to be equal to the following:

$$\frac{dC_{s,holo}}{dt} = k_a L R_s - (k_d + k_{\text{int}}) C_{s,holo} \tag{14}$$

where k_{int} is the rate constant for internalization of the holo-Tf/TfR complexes from the cell surface.

In this experiment, radiolabeled Tf was first allowed to bind to receptors on cells at 4°C in the presence of energy inhibitors to allow equilibrium to be attained while preventing internalization. Unbound ligand was then removed, and medium was added containing excess unlabeled Tf at physiological temperature. In the presence of excess unlabeled ligand, when a radiolabeled ligand dissociates from a receptor, an unlabeled ligand will bind to the receptor. The dissociated radiolabeled ligand is then assumed to not be able to rebind to the receptor due to the excess unlabeled ligand that is present. Accordingly, you are only observing the dissociation of radiolabeled ligand from the cell-surface receptors as you measure the number of radiolabeled ligand/receptor complexes per cell as a function of time (where t=0 corresponds to when the media containing excess unlabeled ligand was added). Under these experimental conditions, Eq. (14) can be simplified to:

$$\frac{dC_{s,holo}}{dt} = -k_d C_{s,holo} \tag{15}$$

Similar to the manipulation between Eqs. (10) and (12), Eq. (15) can be integrated along with the initial condition of $C_{s,holo} = C_{s,holo,0}$ at $t = 0$. Then, letting $t_{1/2}$ be the time at which the number of holo-Tf/TfR surface complexes, $C_{s,holo}$, is equal to one-half the number of surface complexes initially present, $C_{s,holo,0}$, Eq. (16), below, can be derived:

$$t_{1/2} = \frac{\ln(2)}{k_d} \tag{16}$$

Plotting the loss of surface Tf/TfR complexes over time semi-logarithmically, allows for the determination of $t_{1/2}$. The rate constant of holo-Tf dissociation was then determined to be 0.090 min^{-1} using Eq. (16) [98]. In a similar manner, Sainte-Marie and coworkers determined the dissociation rate constant to be 0.056 ± 0.01 min^{-1} [100].

3.2. Internalization and Intracellular Events

3.2.1. Determining the endocytic rate constant for the holo-Tf/TfR complex: Method I—

The rate constant for the endocytosis of the holo-Tf/TfR complex can also be estimated by combining radiolabeling with mathematical modeling. In one method [98], Lodish and coworkers allowed radiolabeled holo-Tf to first bind to cells at 4°C to achieve maximum binding. After removing unbound Tf, medium containing excess unlabeled Tf at physiological temperature was added to facilitate internalization of labeled Tf, in addition to preventing rebinding of dissociated radiolabeled ligand. For this scenario, both dissociation and internalization of Tf must be considered, since both processes are occurring. Therefore Eq. (14) simplifies to:

$$\frac{dC_{s,holo}}{dt} = -(k_d + k_{\text{int}})C_{s,holo} \tag{17}$$

Integrating and rearranging Eq. (17) in a manner similar to what was performed between Eqs. (10) and (12), yields the following:

$$t_{1/2} = \frac{\ln(2)}{(k_d + k_{\text{int}})} \tag{18}$$

The loss of radiolabeled Tf from the cell surface as a function of time was determined by measuring the pronase-sensitive radiolabeled ligand, where pronase corresponds to a mixture of proteases that can cleave and release surface-bound Tf. Creating a semi-logarithmic plot of the fraction of initial Tf bound as a function of time allowed for the determination of the $t_{1/2}$ for the total process of dissociation and internalization of Tf. Using the above equation, k_{int} can be calculated using the $t_{1/2}$ for the process and $k_d = 0.090\ \text{min}^{-1}$, as estimated previously. The rate of internalization was found to be $0.20\ \text{min}^{-1}$ using this approach [98]. Also using the same assumptions, Sainte-Marie and coworkers found k_{int} to be $0.214 \pm 0.01\ \text{min}^{-1}$ [100].

In a similar manner, Young and coworkers evaluated the rate constant for the internalization of the holo-Tf/TfR complex, neglecting the dissociation of holo-Tf from TfR [102]. In this case, the authors measured the percentage of cell-surface complexes remaining prior to endocytosis using pronase to distinguish cell-surface bound from internalized complexes. In this case, Eq. (17) can be written as follows after dividing through by the initial cell-surface complexes, $C_{s,holo,0}$, and neglecting dissociation:

$$\frac{d\left(\frac{C_{s,holo}}{C_{s,holo,0}}\right)}{dt} = -k_{\text{int}}\frac{C_{s,holo}}{C_{s,holo,0}} \tag{19}$$

Similar to the integration and rearrangement performed between Eqs. (10) and (12), using the initial condition of no complexes inside the cell at $t = 0$, and with $t_{1/2}$ occurring when the complexes at the surface are one-half the amount initially present, we have the following relationship:

$$t_{1/2} = \frac{\ln(2)}{k_{\text{int}}} \tag{20}$$

Therefore, the $t_{1/2}$ value can be found from the semi-logarithmic plot of the percentage of cell-surface complexes remaining as a function of time. Equation (20) can then be used to estimate the rate constant for internalization, which was found to be 0.45 min^{-1}.

3.2.2. Determining the endocytic rate constant for the holo-Tf/TfR complex: Method II—The In/Sur plot method, described by Wiley and Cunningham, has also been used to evaluate the endocytic rate constant of the holo-Tf/TfR complex [96]. A species balance on the internalized complexes was performed, where the number of internalized Tf/TfR complexes per cell, C_i, can increase through endocytosis of the cell-surface complexes and can be decreased by recycling to the cell surface and degradation, as described in the following equation:

$$\frac{dC_i}{dt} = k_{\text{int}} C_{s,holo} - k_{rec} C_i + k_{\text{deg}} C_i \tag{21}$$

where k_{rec} is the rate constant for recycling of the complex, and k_{deg} is the rate constant for degradation of the complex.

Using short time periods (under 6 minutes), when linear accumulation of Tf/TfR complexes was observed, the recycling and degradation of the complex could be ignored, giving the following equation:

$$\frac{dC_i}{dt} = k_{\text{int}} C_{s,holo} \tag{22}$$

Integration of Eq. (22), while assuming the number of complexes at the cell surface does not change significantly over the time frame of the experiment, and applying the condition that initially no complexes are present within the cell, $C_i(t = 0) = 0$, results in the following:

$$\frac{C_i}{C_{s,holo}} = k_{\text{int}} t \tag{23}$$

Gironès and Davis measured the accumulation of internalized Tf/TfR complexes using radiolabeled Fab fragments of the monoclonal anti-TfR antibody (OKT9) [103]. The amount of internalized complexes was determined by measuring cell-associated radioactivity following an acid wash to remove surface bound Tf. The surface bound Tf was then calculated by subtracting the internalized Tf from the total specific bound radioactivity. The ratio of internalized complexes to surface bound complexes, $C_i/C_{s,holo}$, was then plotted versus time, and the endocytic rate constant was found from the slope to be 0.22 ± 0.02 min^{-1}. Also using this method, Czech and coworkers found k_{int} to be 0.33 min^{-1} [99].

Another form of the In/Sur plot can also be derived without assuming the number of complexes at the cell surface is constant with time [104]. Solving Eq. (22) using the initial condition of no ligand present inside the cell, results in the following equation:

$$C_i(t) = k_{\text{int}} \int_0^t C_{s,holo}(t)\,dt \tag{24}$$

This form of the In/Sur plot can then be created using measurements of the internalized complex, C_i, and estimating the integral of the surface complex, $C_{s,holo}$, over the time period of interest. Estimation of the integral can be performed using different approaches, such as

the trapezoidal and Simpson's rules. The endocytic rate constant, k_{int}, can be determined from the slope of this graph.

3.2.3. Determining endocytic rate constant for the holo-Tf/TfR complex: Method III—

Iacopetta and Morgan evaluated the rate constant for endocytosis of the holo-Tf/TfR complex using a method previously described for asialoglycoprotein in hepatocytes [71, 105]. For evaluation of internalization, binding of radiolabeled Tf was first allowed to occur at 4°C, and then endocytosis was initiated by adding media at physiological temperature. Experimentally, short time periods were used, allowing recycling and degradation to be neglected in Eq. (21) above, again yielding Eq. (22). Both sides of Eq. (22) were then divided by the initial number of surface complexes, $C_{s,holo,0}$, which is assumed to be constant and can be brought inside the derivative to yield:

$$\frac{d\left(\frac{C_i}{C_{s,holo,0}}\right)}{dt}=k_{\text{int}}\frac{C_{s,holo}}{C_{s,holo,0}} \tag{25}$$

For the short time periods under consideration, it was then assumed that all radiolabeled Tf is either bound to the surface of the cell or present within the cell, and therefore the fraction of complexes at the cell surface, $C_{s,holo}/C_{s,holo,0}$, in Eq. (25) can be expressed in terms of the fraction of complexes inside the cell that were initially present on the cell surface, $C_i/C_{s,holo,0}$. Using this information Eq. (25) can be integrated using the integrating factor, and solving for $C_i/C_{s,holo,0}$, using the initial condition that C_i is equal to zero at $t = 0$, since no radiolabeled complexes are inside the cell at the start of the experiment, yields:

$$\frac{C_i}{C_{s,holo,0}}=1-\exp(-k_{\text{int}}t) \tag{26}$$

Subsequently, as detailed in the Supplementary Information section of this review, Eq. (26) was manipulated to yield the following equation:

$$\ln\left(\frac{C_0-C_1}{C_0-C_2}\right)=k_{\text{int}}(t_2-t_1) \tag{27}$$

where C_0 is 100%, and C_1 and C_2 can be defined as the percentages of internal Tf/TfR complexes relative to the initial amount bound at time t_1 and t_2, respectively.

By measuring the radioactivity of internalized ligand at times t_1 and t_2, the internalization rate constant was found using Eq. (27) to be 0.43 ± 0.07 min^{-1} [71]. Using a similar method, May and Tyler found the rate constant of internalization to be 0.183 min^{-1} [106]. It is noted that while this method utilizes data from only two time points, t_1 and t_2, the use of several data points is generally preferred to determine the rate constant.

3.2.4. Determining the endocytic rate constant for the holo-Tf/TfR complex: Method IV—

Strous and coworkers determined the endocytic rate constant using radiolabeled iron loaded Tf [107]. Since iron is released from Tf inside cells, it was expected that the iron would not recycle from the cell like Tf, and therefore, the rate of accumulation of internalized ^{59}Fe inside the cell could be a measure of the rate of endocytosis. The following species balance was performed on the internalized radiolabeled iron, Fe_i.

$$\frac{dFe_i}{dt} = k_{\text{int}} Fe_s \tag{28}$$

where Fe_s is iron bound to Tf at the cell surface. Using an approach similar to that applied in the integration of Eq. (25), both sides of Eq. (28) was divided by the maximum number of iron atoms that could be internalized, $Fe_{s,0}$, which is the number of radiolabeled iron atoms initially bound to Tf at the cell surface. Subsequently, using the integrating factor to solve the equation with the initial condition of $Fe_i = 0$ at $t = 0$ yields:

$$\frac{Fe_i}{Fe_{s,0}} = 1 - \exp(-k_{\text{int}} t) \tag{29}$$

The half-time of internalization can then be found by rearranging Eq. (29), taking the natural logarithm of both sides, and letting Fe_i equal one-half $Fe_{s,0}$ at $t_{1/2}$.

$$t_{1/2} = \frac{\ln(2)}{k_{\text{int}}} \tag{30}$$

Therefore, the half-time could be determined using a semi-logarithmic plot of the accumulated radiolabeled iron as $(1 - (\text{Fe}_i/\text{Fe}_{s,0}))$ as a function of time. Using Eq. (30), the rate constant for internalization was found to be 0.231 min^{-1}.

Using a similar approach, Glass and coworkers determined the rate of endocytosis of the Tf/TfR complex by measuring the fraction of total complexes internalized over time rather than the accumulation of iron inside the cell [101]. Cells were incubated with excess radiolabeled Tf at 37°C to facilitate internalization. At desired time points, the surface-bound radiolabeled Tf was removed using 200 μL rabbit plasma, and then the number of internalized complexes was determined by measuring cell-associated radioactivity. Equation (21) was simplified assuming no recycling or degradation over short times, and divided through by the initial surface bound complexes, $C_{s,holo,0}$, to yield Eq. (25). Integration of Eq. (25) gives Eq. (26). Finally, Eq. (30) was derived, as shown between Eq. (29) and (30), where $t_{1/2}$ is the time when $C_i = ½C_{s,0}$. This equation was then used to calculate the internalization rate constant using the $t_{1/2}$ value found from a semi-logarithmic plot of the fraction of total receptors internalized versus time. Using this method, k_{int} was found to be 0.84 min^{-1}.

3.2.5. Arrhenius Equation—The activation energy, E_a, for the rate constant for internalization of the holo-Tf/TfR complex can be determined using an Arrhenius plot. The Arrhenius equation, which describes the strong temperature dependence of the internalization rate constant, is given by:

$$k_{\text{int}} = A \exp\left(-\frac{E_a}{RT}\right) \tag{31}$$

where A is the pre-exponential factor, R is the ideal gas constant, and T is the absolute temperature. The term $exp(-E_a/(RT))$ can be interpreted as the fraction of collisions between reactant molecules that have the minimum energy, E_a.

Again referring to Eq. (22), Tf was allowed to bind TfR using short incubation times, in order to assume negligible recycling and degradation of the complex. Rearranging this equation to solve for the internalization rate constant yields:

$$k_{\text{int}} = \frac{\frac{dC_i}{dt}}{C_s} \tag{32}$$

It was then assumed that the Tf/TfR complexes at the surface, C_s, remained constant over short time periods with excess radiolabeled ligand present, although it should be noted that C_s can rapidly change. Nevertheless, substituting Eq. (32) into Eq. (31), then taking the natural logarithm and rearranging, results in the following:

$$ln\left(\frac{dC_i}{dt}\right) = -\frac{E_a}{R}\frac{1}{T} + ln\,(AC_s) \tag{33}$$

In order to determine the rate of endocytosis, dC_i/dt, Iacopetta and Morgan measured internalized radiolabeled Tf as a function of time for different temperatures [71]. The rate was determined by performing linear regression of the plot of internalized radiolabeled Tf versus time using short time points prior to reaching steady-state between endocytosis and exocytosis, when the internalization of Tf proceeded linearly with time. Using this technique, the rate of endocytosis was found to occur at 500 molecules/cell/s at physiological temperature.

Equation (33) was then used to estimate the activation energy from the slope of the semi-logarithmic plot of the rate of endocytosis, dC_i/dt, as a function of the inverse of the absolute temperature. The apparent activation energy of endocytosis was 33.0 ± 2.7 kcal/mol below 26.4 ± 0.4 °C and 12.3 ± 1.6 kcal/mol at higher temperatures [71]. The activation energy for endocytosis was lower at higher temperatures, indicating potentially a smaller amount of energy to overcome for endocytosis to occur at higher temperatures.

3.2.6. Scatchard Analysis and SPR – endosomal binding affinity of apo-Tf for TfR—

Scatchard analysis and SPR was used to evaluate the binding affinity of apo-Tf/TfR inside the endosome. Using low temperatures to prevent internalization, the binding of apo-Tf to TfR was evaluated under acidic conditions to mimic endosomal conditions. Experimentally, HepG2 cells were incubated with radiolabeled Tf at pH 5.4, which would facilitate the release of iron from Tf at the cell surface. The free iron was sequestered by an iron chelator, desferrioxamine, preventing the reformation of holo-Tf. Scatchard analysis showed that the number of Tf binding sites per cell to be 58,000 and that apo-Tf binds its receptor with a K_D of 13 nM under these conditions. It was therefore found that at an acidic pH reflecting that of the endosome, apo-Tf binds with the same affinity and to the same extent as holo-Tf at pH 7.0, and therefore it was assumed that Tf remains bound to its receptor after releasing iron [108]. Using SPR, Bjorkman and coworkers also found a high affinity of apo-Tf for TfR at endosomal pH using two methods [93]. In the first method, equilibrium binding data were used, and the K_D was found to be <15 nM. The second method determined the K_D using a ratio of the kinetic parameters as shown in Eq. (8), which are the endosomal association constant, $k_{a,end}$, and endosomal dissociation constant, $k_{d,end}$. With this approach, the equilibrium dissociation constant was found to be 1.3 nM using a $k_{a,end}$ value of 4.4 ± 0.4 × 10^7 min^{-1} M^{-1} and a $k_{d,end}$ value of 0.056 ± 0.012 min^{-1}. Accordingly, the SPR data supported the conclusion that apo-Tf remains bound to its receptor inside the endosome following release of iron.

3.3. Recycling and Release of Apo-Transferrin

3.3.1. Determining recycling rate constant for apo-Tf/TfR complex: Method I—

Lodish and coworkers determined the rate constant for the appearance of internalized apo-Tf

at the cell surface, k_{rec}, using species balances on all components, along with the rate constants for the other steps that were predetermined with the above-mentioned experiments [98]. They varied the value for k_{rec} until they were able to find the best-fit to their experimental results of the surface, internal, and exocytosed ligand as a function of time. Based on this approach, k_{rec} was found to be 0.139 min^{-1}. It should be noted that in the Lodish paper, the recycling rate constant is a combination of the iron release rate constant and exocytosis constant, since they were not able to separate the two processes. However, since this paper was published, technological advances have enabled researchers to determine the rate constant for iron dissociation from Tf, and another chapter in this special issue discusses iron release from Tf in more detail.

3.3.2. Determining recycling rate constant for apo-Tf/TfR complex: Method II—

Iacopetta and Morgan used a pulse-chase technique to determine the recycling rate constant for the apo-Tf/TfR complex [71]. Initially, Tf was incubated with cells at 37°C to achieve maximum cell-associated Tf and steady-state. Subsequently, 50-fold excess unlabeled Tf was added to "chase" the radiolabeled Tf already internalized from the cell. Equation (21) was simplified assuming no endocytosis or degradation, since no further internalization of radiolabeled Tf was expected in the presence of excess unlabeled ligand.

$$\frac{dC_i}{dt} = -k_{rec}C_i \tag{34}$$

Integrating both sides of the above equation using the initial number of complexes inside the cell as $C_i(t = 0)$, and taking the natural logarithm of both sides gives the following:

$$\ln(C_i) = -k_{rec}t + \ln(C_i(t=0)) \tag{35}$$

Performing linear regression of the semi-logarithmic plot of the loss of intracellular Tf over time, measured as pronase-resistant cell-associated radioactivity, the recycling rate constant, k_{rec}, can be determined from the slope. Using the method shown above, the recycling rate constant at 37 °C was calculated to be 0.48 min^{-1} [71].

3.3.3. Determining recycling rate constant for apo-Tf/TfR complex: Method III

—Sugiyama and coworkers also evaluated the recycling rate constant for the apo-Tf/TfR complex [109] by first performing a species balance on apo-Tf cell-surface complexes. Since surface bound Tf was removed after allowing internalization to occur, labeled ligand was not allowed to internalize after $t = 0$. In addition, medium with an acidic pH was applied after $t = 0$ to inhibit dissociation of apo-Tf from TfR. Accordingly, the species balance can be simplified to:

$$\frac{dC_{s,apo}}{dt} = k_{rec}C_i \tag{36}$$

where $C_{s,apo}$ would then represent the recycled apo-Tf/TfR complex from the cell's interior present on the cell surface. The above equation can then be integrated from 0 to 120 minutes, where $C_{s,apo} = 0$ at $t = 0$, since the surface complexes were removed at the start of the experiment.

$$C_{s,apo}(t=120) = k_{rec}\int_0^{120} C_i dt \tag{37}$$

As detailed in the Supplementary Information section, evaluation of the integral of C_i in the right-hand side of Eq. (37) allowed the derivation of the following expression for the recycling rate constant, k_{rec}.

$$k_{rec}=\frac{C_{s,apo}(t=120)}{\left[\frac{120\cdot[\{C_i(t=0)\}-\{C_i(t=120)\}]}{ln\{C_i(t=0)\}-ln\{C_i(t=120)\}}\right]} \tag{38}$$

where $C_{s,apo}(t = 120)$, is the number of complexes at the surface after 120 min, $C_i(t = 0)$ is the initial number of internalized complexes, assuming internalization and degradation of the ligand were negligible, and $C_i(t = 120)$ is the number of complexes present in the cell after 120 min.

Using this method, the recycling rate constant, k_{rec}, was found to be approximately 0.02 min^{-1} [109]. It should be noted that while Eq. (38) is calculated using only two time points, using more data points is preferred.

3.3.4. Determining recycling rate constant for apo-Tf/TfR complex: Method IV

—Strous and coworkers determined the rate constant for exocytosis in a manner similar to the approach used by Lodish and coworkers to determine the rate constant for binding and dissociation of holo-Tf from the cell surface [107]. First, cells were incubated with a saturating amount of radiolabeled Tf, so that when the system reached steady-state, all receptors were assumed to be occupied. Further internalization was then inhibited using low temperatures, and surface bound ligand was removed using an acid wash to prevent internalization of labeled ligand. Therefore, Eq. (21) was simplified to Eq. (34) assuming no endocytosis or degradation. The temperature was subsequently raised to allow trafficking to occur in the presence of excess unlabeled Tf.

Similar to the manipulation detailed above between Eqs. (10) and (12), Eq. (34) was integrated and solved with the initial condition of $C_i = C_i(t = 0)$ at $t = 0$. In addition, letting $t_{1/2}$ be the time at which the number of internalized complexes is equal to one-half the number of surface complexes initially present, Eq. (39) below can be derived.

$$t_{1/2}=\frac{\ln(2)}{k_{rec}} \tag{39}$$

The half-life could be determined by creating a semi-logarithmic plot of the loss of radiolabeled Tf from inside the cell as a percentage of the maximum value over time. Subsequently, using Eq. (39), the recycling rate constant, k_{rec}, was found to be 0.060 min^{-1}. With the same approach May and Tyler determined the recycling rate constant to be 0.113 min^{-1} [106].

In a similar manner, Young and coworkers found the rate of recycling using the loss of cell-associated radiolabeled complexes as a percentage of the initial, or maximum, amount of Tf bound [102]. Therefore, Eq. (34) could be written as follows, assuming only recycling of the Tf/TfR complex in the presence of excess unlabeled Tf:

$$\frac{d\left(\frac{C_i}{C_{\max}}\right)}{dt}=-k_{rec}\frac{C_i}{C_{\max}} \tag{40}$$

Equation (40) was solved to yield Eq. (39) with an approach similar to the manipulation between Eqs. (10) and (12), using the initial condition of $C_i = C_i(t = 0)$ at $t = 0$ and letting $t_{1/2}$ be the time at which the number of internalized complexes was equal to one-half the maximum number of cell-associated complexes, C_{max}. Subsequently, by creating a semi-logarithmic plot of the percentage of internalized Tf remaining in the cell versus time, the $t_{1/2}$ can be found, and therefore, the k_{rec} using Eq. (39). In this paper, the exocytosis rate constant was found to be 0.1 min^{-1}. Also using this method, Czech and coworkers found the recycling rate constant to be 0.11 min^{-1} [99].

3.3.5. Determining recycling rate constant for apo-Tf/TfR complex: Method V— Using steady-state conditions, Sainte-Marie and coworkers determined the recycling rate constant [100]. Saturating levels of radiolabeled Tf were incubated with cells and allowed to reach steady-state, i.e., when the total, cell-surface bound, and internal radioactivity no longer changed with time. Since saturating levels of Tf were used, it was assumed that degradation could be neglected and that there were no free internalized receptors. In this experiment, the total number of receptors, R_T, was assumed to include the number of free cell-surface receptors, R_s, the number of receptors bound to holo-Tf at the surface, $C_{s,holo}$, as well as, the number of receptors bound to holo- and apo-Tf within the cell, C_i..

Equations (14) and (21) were then set to zero, since steady-state had been attained, and solved for k_{int} and k_{rec}, respectively. Combining these equations and replacing R_s in terms of R_T, $C_{s,holo}$, and C_i, yields the following expression for the recycling rate constant:

$$k_{rec} = \frac{k_a L}{k_d}\left[\frac{R_T - C_{s,holo} - C_i}{C_i}\right] \tag{41}$$

Accordingly, by measuring the total, cell-surface bound, and internal radioactivity under steady-state conditions, and using the k_a and k_d found earlier from binding experiments, the k_{rec} was found to be 0.19 ± 0.03 min^{-1}.

3.3.6. Determining recycling rate constant for apo-Tf/TfR complex: Method VI —Gironès and Davis determined the exocytosis rate constant by fitting the loss of cell-associated Tf experimental data to a double exponential decay model using the computer program ENZFITTER (Elsevier Biosoft) [103]. Cells were first incubated with radiolabeled Fab fragments for TfR for 5 min at 37°C in the presence of holo-Tf. The temperature was then reduced to 4°C, and the surface bound radiolabeled antibody was removed. Subsequently, the loss of cell-associated radioactivity was measured over time. This data was then fit to a single exponential decay and a double exponential decay model to determine the rate constant for recycling of Tf. Using the F test to determine the quality of the fit, the double exponential decay model was statistically found to better predict the experimental data ($P < 0.001$). Using the double exponential decay model, k_{rec} was found to be 0.065 ± 0.002 min^{-1}.

3.3.7. Determination of rate constant for dissociation of apo-Tf from the cell surface—Lodish and coworkers also estimated the rate constant for the dissociation of apo-Tf from its receptor at the cell surface, $k_{d,apo}$, by combining a radioactivity experiment with mathematical modeling [98]. Holo-Tf was incubated with cells at 4°C and pH 7.3, which facilitated binding, but prevented internalization. Then apo-Tf was produced by removing iron at pH 5.0 in the presence of desferrioxamine, a potent iron chelator, which prevented the rebinding of iron. Next, energy inhibitors were used to prevent internalization, while the pH was again raised to pH 7.3. Under these experimental conditions, the species balance on the number of apo-Tf/TfR complexes is given by the following equation:

$$\frac{dC_{s,apo}}{dt} = -k_{d,apo}C_{s,apo} \tag{42}$$

Integrating and rearranging Eq. (42), in an approach similar to what was used between Eqs. (10) and (12), yields the following:

$$t_{1/2} = \frac{\ln(2)}{k_{d,apo}} \tag{43}$$

In this study, Lodish and coworkers plotted the cell-surface apo-Tf as a function time, and determined $t_{1/2}$ for the dissociation of apo-Tf at neutral pH to be 16 s [98]. Using Eq. (43), the $k_{d,apo}$ value was found to be 2.6 min^{-1}. It was concluded that apo-Tf rapidly dissociates from the cell surface following exocytosis. Using a similar approach, Czech and coworkers also found the rate constant for dissociation of apo-Tf from the cell-surface receptors to be the same value of 2.6 min^{-1} [99].

3.4. Determining kinetic rate constant parameters by fitting data to models

Yazdi and Murphy utilized a model similar to Lodish and coworkers [98], except the authors accounted for nonspecific binding and considered the recycling and dissociation of apo-Tf to occur as one step [110]. For nonspecific binding of Tf to the cell surface, the following species balance was derived:

$$\frac{dC_{ns}}{dt} = \frac{N_a}{N_c}k_{a,ns}L - k_{d,as}C_{ns} \tag{44}$$

where C_{ns} is molecules per cell of Tf nonspecifically bound to the cell surface, N_a is Avogadro's number in number/mol, N_c is the cell concentration in cells/L, $k_{a,ns}$ is the pseudo-first order rate constant for ligand nonspecifically binding to the cell membrane, $k_{d,ns}$ is the rate constant for ligand dissociating from the cell membrane, and L is the free ligand (Tf) concentration in M.

Since the nonspecific binding was assumed to be at a constant level at all times, Eq. (44) was set equal to zero, and solved for C_{ns}.

$$C_{ns} = \frac{N_a}{N_c}\frac{k_{a,ns}}{k_{d,ns}}L \tag{45}$$

where the ligand concentration was assumed to be constant throughout the experiment at 7.8×10^{-9} M, and the ratio of $k_{a,ns}/k_{d,ns}$ was found to be $(1.4 \pm 0.1) \times 10^{-3}$ based on results from a steady-state experiment (where $C_{s,holo}$ and C_i were allowed to reach steady-state).

The following species balance was written for Tf specifically bound to TfR, where the free receptors can be written as the total number of cell-surface receptors, $R_{S,T}$, minus the number of complexes, $C_{s,holo}$:

$$\frac{dC_{s,holo}}{dt} = k_a L\left(R_{s,T} - C_{s,holo}\right) - (k_d + k_{\text{int}})C_{s,holo} \tag{46}$$

A species balance was also performed on the number of internalized Tf/TfR complexes:

$$\frac{dC_i}{dt} = k_{\text{int}} C_{s,holo} - k_{rec+d,apo} C_i \tag{47}$$

where $k_{rec+d,apo}$ is the lumped rate constant for recycling and dissociation of apo-Tf. Note that apo-Tf was not considered as a species in the equation, since $k_{rec+d,apo}$ included dissociation of apo-Tf from TfR.

Finally, a balance on the total number of cell-associated radiolabeled Tf, C_{total}, was performed.

$$C_{total} = C_{s,holo} + C_{ns} + C_i \tag{48}$$

In this experiment, cells were incubated with radiolabeled Tf and the total, surface bound, and internal radioactivity was measured over time. The kinetic parameters were then determined by fitting the Eqs. (45) through (48) to the experimental data of surface, total, and internalized radiolabeled Tf, using a general purpose regression program GREG in multiresponse mode in combination with DDASAC software package to estimate the ordinary differential equations. GREG uses the modified Newton's method, starting from user-input initial guesses for the parameters, and then convergence is reached when Newton corrections of estimated parameters were no larger than 0.1 times their respective uncertainties. Additionally, DDASAC uses a predictor-corrector investigation program to solve systems of coupled ODE's and algebraic equations. Using this method, the following rate constants were determined: $k_a = (4 \pm 1) \times 10^7$ min^{-1} M^{-1}, $k_d = 1.3 \pm 0.5$ min^{-1}, $k_{int} = 0.38 \pm 0.05$ min^{-1}, and $k_{rec+d,apo} = 0.18 \pm 0.02$ min^{-1}.

3.5. Calculation of Tf cycle time

Multiple methods have also been used to estimate the Tf cycle time. Lodish and coworkers calculated the total time to complete one cycle of the Tf trafficking pathway, T_c, as the sum of the characteristic time constants for each of the steps, i.e., the inverse of the rate constant for the association of Tf to TfR times the ligand concentration, k_aL; the internalization rate constant, k_{int}; the recycling rate constant, k_{rec}; and the dissociation rate constant for apo-Tf, $k_{d,apo}$.

$$T_c = (k_a L)^{-1} + (k_{\text{int}})^{-1} + (k_{res})^{-1} + \left(k_{d,apo}\right)^{-1} \tag{49}$$

Using this expression, the cycle time was found to be approximately 15.8 min [98]. Similarly, using Eq. (49), Strous and coworkers calculated T_c to be 22.7 min when they used their own experimentally determined rate constants k_{int} and k_{rec}, along with the k_a and k_d values determined by Lodish and coworkers [98, 107].

Sainte-Marie and coworkers modified Eq. (49) by removing the rate constant for dissociation of apo-Tf, since this was expected to be very large in comparison to the other rate constants considered, and including the rate constant for the transport of unoccupied receptors back to the cell surface, k_R, which was determined to be 0.17 ± 0.08 min^{-1} [100]. The modified equation is shown below:

$$T_c = \left[(k_a L)^{-1} + (k_{\text{int}})^{-1} + (k_{rec})^{-1} + (k_R)^{-1} \right] - \left[(k_R)^{-1} \cdot \frac{R_s}{R_T} \right] \tag{50}$$

where R_s/R_T was 0.5. Using this method, the cycle time was found to be 14 min.

Nunez and Glass, on the other hand, estimated the total time for transferrin to complete its cycle as 4 min [111]. In their experiment, the cells were incubated with ^{59}Fe-^{125}I-Tf for a 10 s pulse, followed by a chase with excess unlabeled Tf. At desired time points, trafficking was halted using a cold wash of the cells, and the amount of cell associated Tf and Fe was measured (Figure 8). As shown in the figure, Tf is not released from the cell for approximately 60 s. The amount of Tf then decreases over time, while iron remains within the cell. The half-time of release was found to be 110 ± 14 s after the initial 60 s lag period, and the entire trafficking cycle was found to be completed within 260 ± 39 s.

Similarly, using a pulse-chase approach, Watkins and coworkers calculated the cycle time using the following equation [101].

$$T_c = \frac{t_0}{R\left(\frac{Fe}{I}\right)_{cell} / R\left(\frac{Fe}{I}\right)_{Tf}} \tag{51}$$

where t_0 is the time ^{59}Fe-^{125}I labeled Tf is allowed to incubate with the cells, $R(Fe/I)_{cell}$ is the ratio of ^{59}Fe to ^{125}I radioactivity associated with the cell after t_0 minutes of incubation, and $R(Fe/I)_{Tf}$ is the ratio of ^{59}Fe to ^{125}I radioactivity in the iron-saturated ^{59}Fe-^{125}I-labeled Tf. It was assumed that after the first Tf trafficking cycle, two iron atoms are delivered per one Tf that is internalized. Therefore, to estimate this ratio that would be present after the first cycle, $R(Fe/I)_{Tf}$ was used, since it was measured by considering a solution of iron saturated Tf. Since the authors found that the amount of ^{125}I-Tf inside the cells became fixed after 5–10 minutes, any additional Tf trafficking cycles would be expected to only increase the ^{59}Fe pool within the cell. As a result, taking the ratio of ^{59}Fe to ^{125}I within the cell, $R(Fe/I)_{cell}$, after t_0 minutes and dividing by $R(Fe/I)_{Tf}$, which is used to represent the initial ratio, will give the number of cycles completed within the incubation time. Using this method, T_c was found to be 255 ± 43 sec, or approximately 4.25 min.

3.6. Identifying design criteria for drug delivery using mathematical models

These rate constants have also been used to help engineer Tf mutants that are more effective in delivering anticancer drugs. Specifically, TfR is overexpressed on several cancers, since they require more iron to sustain their rapid proliferation. Accordingly, Tf has been used to selectively target cancer cells. However, as mentioned in this review, Tf recycles very rapidly, and this short duration inside the cell can limit the ability of Tf to deliver its cytotoxic payload. In order to improve the ability of Tf to deliver its conjugated drug, Kamei and coworkers developed a mathematical model of the intracellular trafficking pathway of Tf, and used a sensitivity analysis to determine a novel design criterion for improving the drug delivery efficacy of Tf [112]. Specifically, if the iron release rate of Tf within the endosome is reduced, iron would be retained by Tf upon recycling to the cell surface. Since the affinity of holo-Tf for TfR is high, the Tf-drug conjugate would be reinternalized to participate in another cycle of trafficking. The probability of Tf delivering its drug would therefore be improved, since multiple rounds of trafficking would occur. With this design criterion, Kamei and coworkers investigated two Tf mutants with decreased endosomal iron release rates [113–114]. These Tf mutants were conjugated to diphtheria toxin (DT) and shown to more effectively deliver DT *in vitro* to U87 and U251 human glioma cell lines when compared with wild type. In addition, these Tf-DT conjugates were administered to U87-derived tumors grown on the flanks of mice. In these *in vivo* experiments, the administration of the mutant Tf-DT conjugates led to rapid and near complete tumor regression, while the wild-type Tf-DT conjugates only suppressed tumor growth (Figure 9). Further studies are currently ongoing to assess this technology, which has potential since

wild-type Tf conjugated to a mutant of DT reached phase III clinical trials for the treatment of glioblastoma multiforme [115–117].

4. Concluding Remarks

Various techniques have been employed to investigate the intracellular trafficking pathway of Tf including the machinery components and regulators involved. The roles of various mediators have been experimentally studied through qualitative methods such as TIRF microscopy, electron microscopy, laser-scanning confocal fluorescence microscopy, and spinning-disk confocal fluorescence microscopy. These techniques have temporal resolution and are useful for the imaging of Tf endocytosis and recycling which occur on the order of seconds to minutes.

TIRF microscopy can be utilized to visualize events occurring near the cell surface, such as vesicle formation during clathrin-mediated endocytosis. Electron microscopy similarly is primarily used to visualize clathrin-coated pits and vesicles near the cell surface. On the other hand, confocal fluorescence microscopy can examine the presence of Tf within early endosomes, throughout the cytoplasm, and in recycling endosomes concentrated near the perinuclear region. Experiments utilizing these techniques have shown that Tf is internalized through clathrin-mediated endocytosis and initially trafficked indiscriminately to both populations of static and dynamic early endosomes. Subsequent sorting of cargo within early endosomes induces tubular formations to separate and shuttle Tf either to recycling endosomes within the perinuclear region of the cell, or directly back to the cell surface at the plasma membrane.

Additionally, radiolabeling techniques when combined with mathematical modeling have enabled researchers to evaluate the kinetic parameters and equilibrium dissociation constants associated with Tf binding and trafficking. Several different mathematical models have been discussed in this review, which have used simplifying assumptions to allow integration and estimation of parameters from experimental data. Equilibrium dissociation constants can also be evaluated using extended incubation times in the radioactivity experiments to ensure equilibrium between binding and dissociation. Another more advanced technique to evaluate the binding and dissociation of Tf is SPR. By adjusting the experimental procedure, SPR can be used to evaluate kinetic, as well as equilibrium, binding and dissociation events. In conclusion, both qualitative and quantitative data can be used to obtain valuable information about the transferrin pathway, which in turn, can be used to identify design parameters to improve the ability of transferrin to deliver anti-cancer agents.

Supplementary Material

Refer to Web version on PubMed Central for supplementary material.

Acknowledgments

The authors would like to thank the support of the UCSF Brain Tumor Specialized Program of Research Excellence NIH P50CA097257.

References

1. Pearse BM, Robinson MS. Clathrin, adaptors, and sorting. Annu Rev Cell Biol. 1990; 6:151–171. [PubMed: 2177341]
2. Calzolari A, Larocca LM, Deaglio S, Finisguerra V, Boe A, Raggi C, Ricci-Vitani L, Pierconti F, Malavasi F, De Maria R, Testa U, Pallini R. Transferrin receptor 2 is frequently and highly expressed in glioblastomas. Transl Oncol. 2010; 3:123–134. [PubMed: 20360937]

3. Trinder D, Baker E. Transferrin receptor 2: a new molecule in iron metabolism. Int J Biochem Cell Biol. 2003; 35:292–296. [PubMed: 12531241]
4. Deaglio S, Capobianco A, Cali A, Bellora F, Alberti F, Righi L, Sapino A, Camaschella C, Malavasi F. Structural, functional, and tissue distribution analysis of human transferrin receptor-2 by murine monoclonal antibodies and a polyclonal antiserum. Blood. 2002; 100:3782–3789. [PubMed: 12393650]
5. Lesnikov V, Gorden N, Fausto N, Spaulding E, Campbell J, Shulman H, Fleming RE, Deeg HJ. Transferrin fails to provide protection against Fas-induced hepatic injury in mice with deletion of functional transferrin-receptor type 2. Apoptosis. 2008; 13:1005–1012. [PubMed: 18561026]
6. Graham RM, Reutens GM, Herbison CE, Delima RD, Chua AC, Olynyk JK, Trinder D. Transferrin receptor 2 mediates uptake of transferrin-bound and non-transferrin-bound iron. J Hepatol. 2008; 48:327–334. [PubMed: 18083267]
7. Gruenberg J, Stenmark H. The biogenesis of multivesicular endosomes. Nat Rev Mol Cell Biol. 2004; 5:317–323. [PubMed: 15071556]
8. Lakadamyali M, Rust MJ, Zhuang X. Ligands for clathrin-mediated endocytosis are differentially sorted into distinct populations of early endosomes. Cell. 2006; 124:997–1009. [PubMed: 16530046]
9. Leonard D, Hayakawa A, Lawe D, Lambright D, Bellve KD, Standley C, Lifshitz LM, Fogarty KE, Corvera S. Sorting of EGF and transferrin at the plasma membrane and by cargo-specific signaling to EEA1-enriched endosomes. J Cell Sci. 2008; 121:3445–3458. [PubMed: 18827013]
10. Schweitzer JK, Sedgwick AE, D'Souza-Schorey C. ARF6-mediated endocytic recycling impacts cell movement, cell division and lipid homeostasis. Semin Cell Dev Biol. 2011; 22:39–47. [PubMed: 20837153]
11. Ghosh RN, Gelman DL, Maxfield FR. Quantification of low density lipoprotein and transferrin endocytic sorting HEp2 cells using confocal microscopy. J Cell Sci. 1994; 107(Pt 8):2177–2189. [PubMed: 7983176]
12. Baravalle G, Schober D, Huber M, Bayer N, Murphy RF, Fuchs R. Transferrin recycling and dextran transport to lysosomes is differentially affected by bafilomycin, nocodazole, and low temperature. Cell Tissue Res. 2005; 320:99–113. [PubMed: 15714281]
13. Conner SD, Schmid SL. Regulated portals of entry into the cell. Nature. 2003; 422:37–44. [PubMed: 12621426]
14. Grant BD, Donaldson JG. Pathways and mechanisms of endocytic recycling. Nat Rev Mol Cell Biol. 2009; 10:597–608. [PubMed: 19696797]
15. Nesterov A, Carter RE, Sorkina T, Gill GN, Sorkin A. Inhibition of the receptor-binding function of clathrin adaptor protein AP-2 by dominant-negative mutant mu2 subunit and its effects on endocytosis. Embo J. 1999; 18:2489–2499. [PubMed: 10228163]
16. Robinson MS. The role of clathrin, adaptors and dynamin in endocytosis. Curr Opin Cell Biol. 1994; 6:538–544. [PubMed: 7986531]
17. Marsh M, McMahon HT. The structural era of endocytosis. Science. 1999; 285:215–220. [PubMed: 10398591]
18. Schein S. Architecture of clathrin fullerene cages reflects a geometric constraint--the head-to-tail exclusion rule--and a preference for asymmetry. J Mol Biol. 2009; 387:363–375. [PubMed: 19356592]
19. Bonifacino JS, Traub LM. Signals for sorting of transmembrane proteins to endosomes and lysosomes. Annu Rev Biochem. 2003; 72:395–447. [PubMed: 12651740]
20. Brodsky FM, Chen CY, Knuehl C, Towler MC, Wakeham DE. Biological basket weaving: formation and function of clathrin-coated vesicles. Annu Rev Cell Dev Biol. 2001; 17:517–568. [PubMed: 11687498]
21. Macia E, Ehrlich M, Massol R, Boucrot E, Brunner C, Kirchhausen T. Dynasore, a cell-permeable inhibitor of dynamin. Dev Cell. 2006; 10:839–850. [PubMed: 16740485]
22. Holstein SE, Ungewickell H, Ungewickell E. Mechanism of clathrin basket dissociation: separate functions of protein domains of the DnaJ homologue auxilin. J Cell Biol. 1996; 135:925–937. [PubMed: 8922377]

23. Hill TA, Gordon CP, McGeachie AB, Venn-Brown B, Odell LR, Chau N, Quan A, Mariana A, Sakoff JA, Chircop M, Robinson PJ, McCluskey A. Inhibition of dynamin mediated endocytosis by the dynoles--synthesis and functional activity of a family of indoles. J Med Chem. 2009; 52:3762–3773. [PubMed: 19459681]
24. Quan A, McGeachie AB, Keating DJ, van Dam EM, Rusak J, Chau N, Malladi CS, Chen C, McCluskey A, Cousin MA, Robinson PJ. Myristyl trimethyl ammonium bromide and octadecyl trimethyl ammonium bromide are surface-active small molecule dynamin inhibitors that block endocytosis mediated by dynamin I or dynamin II. Mol Pharmacol. 2007; 72:1425–1439. [PubMed: 17702890]
25. Ehrlich M, Boll W, Van Oijen A, Hariharan R, Chandran K, Nibert ML, Kirchhausen T. Endocytosis by random initiation and stabilization of clathrin-coated pits. Cell. 2004; 118:591–605. [PubMed: 15339664]
26. Pawley, JB. Handbook of Biological Confocal Microscopy. Springer-Verlag US; Boston, MA: 2006. SpringerLink (Online service).
27. Motley A, Bright NA, Seaman MN, Robinson MS. Clathrin-mediated endocytosis in AP-2-depleted cells. J Cell Biol. 2003; 162:909–918. [PubMed: 12952941]
28. Conner SD, Schmid SL. Differential requirements for AP-2 in clathrin-mediated endocytosis. J Cell Biol. 2003; 162:773–779. [PubMed: 12952931]
29. Di Paolo G, De Camilli P. Phosphoinositides in cell regulation and membrane dynamics. Nature. 2006; 443:651–657. [PubMed: 17035995]
30. Zoncu R, Perera RM, Sebastian R, Nakatsu F, Chen H, Balla T, Ayala G, Toomre D, De Camilli PV. Loss of endocytic clathrin-coated pits upon acute depletion of phosphatidylinositol 4,5-bisphosphate. Proc Natl Acad Sci U S A. 2007; 104:3793–3798. [PubMed: 17360432]
31. Roth MG. Phosphoinositides in constitutive membrane traffic. Physiol Rev. 2004; 84:699–730. [PubMed: 15269334]
32. Varnai P, Thyagarajan B, Rohacs T, Balla T. Rapidly inducible changes in phosphatidylinositol 4,5-bisphosphate levels influence multiple regulatory functions of the lipid in intact living cells. J Cell Biol. 2006; 175:377–382. [PubMed: 17088424]
33. Abe N, Inoue T, Galvez T, Klein L, Meyer T. Dissecting the role of PtdIns(4,5)P2 in endocytosis and recycling of the transferrin receptor. J Cell Sci. 2008; 121:1488–1494. [PubMed: 18411250]
34. Rohde G, Wenzel D, Haucke V. A phosphatidylinositol (4,5)-bisphosphate binding site within mu2-adaptin regulates clathrin-mediated endocytosis. J Cell Biol. 2002; 158:209–214. [PubMed: 12119359]
35. Gaidarov I, Keen JH. Phosphoinositide-AP-2 interactions required for targeting to plasma membrane clathrin-coated pits. J Cell Biol. 1999; 146:755–764. [PubMed: 10459011]
36. Suh BC, Inoue T, Meyer T, Hille B. Rapid chemically induced changes of PtdIns(4,5)P2 gate KCNQ ion channels. Science. 2006; 314:1454–1457. [PubMed: 16990515]
37. Axelrod D. Total internal reflection fluorescence microscopy in cell biology. Traffic. 2001; 2:764–774. [PubMed: 11733042]
38. Merrifield CJ, Feldman ME, Wan L, Almers W. Imaging actin and dynamin recruitment during invagination of single clathrin-coated pits. Nat Cell Biol. 2002; 4:691–698. [PubMed: 12198492]
39. Cao H, Chen J, Krueger EW, McNiven MA. SRC-mediated phosphorylation of dynamin and cortactin regulates the “constitutive” endocytosis of transferrin. Mol Cell Biol. 2010; 30:781–792. [PubMed: 19995918]
40. Yashunsky V, Shimron S, Lirtsman V, Weiss AM, Melamed-Book N, Golosovsky M, Davidov D, Aroeti B. Real-time monitoring of transferrin-induced endocytic vesicle formation by mid-infrared surface plasmon resonance. Biophys J. 2009; 97:1003–1012. [PubMed: 19686647]
41. Kruchten AE, McNiven MA. Dynamin as a mover and pincher during cell migration and invasion. J Cell Sci. 2006; 119:1683–1690. [PubMed: 16636070]
42. Head JA, Jiang D, Li M, Zorn LJ, Schaefer EM, Parsons JT, Weed SA. Cortactin tyrosine phosphorylation requires Rac1 activity and association with the cortical actin cytoskeleton. Mol Cell Biol. 2003; 14:3216–3229.
43. Gastaldelli M, Imelli N, Boucke K, Amstutz B, Meier O, Greber UF. Infectious adenovirus type 2 transport through early but not late endosomes. Traffic. 2008; 9:2265–2278. [PubMed: 18980614]

44. Eyster CA, Higginson JD, Huebner R, Porat-Shliom N, Weigert R, Wu WW, Shen RF, Donaldson JG. Discovery of new cargo proteins that enter cells through clathrin-independent endocytosis. Traffic. 2009; 10:590–599. [PubMed: 19302270]
45. Rink J, Ghigo E, Kalaidzidis Y, Zerial M. Rab conversion as a mechanism of progression from early to late endosomes. Cell. 2005; 122:735–749. [PubMed: 16143105]
46. Maxfield FR, McGraw TE. Endocytic recycling. Nat Rev Mol Cell Biol. 2004; 5:121–132. [PubMed: 15040445]
47. Desclozeaux M, Venturato J, Wylie FG, Kay JG, Joseph SR, Le HT, Stow JL. Active Rab11 and functional recycling endosome are required for E-cadherin trafficking and lumen formation during epithelial morphogenesis. Am J Physiol Cell Physiol. 2008; 295:C545–556. [PubMed: 18579802]
48. Gu J, Faundez V, Werner E. Endosomal recycling regulates Anthrax Toxin Receptor 1/Tumor Endothelial Marker 8-dependent cell spreading. Exp Cell Res. 2010; 316:1946–1957. [PubMed: 20382142]
49. Liebl D, Difato F, Hornikova L, Mannova P, Stokrova J, Forstova J. Mouse polyomavirus enters early endosomes, requires their acidic pH for productive infection, and meets transferrin cargo in Rab11-positive endosomes. J Virol. 2006; 80:4610–4622. [PubMed: 16611921]
50. Ullrich O, Reinsch S, Urbe S, Zerial M, Parton RG. Rab11 regulates recycling through the pericentriolar recycling endosome. J Cell Biol. 1996; 135:913–924. [PubMed: 8922376]
51. Eggers CT, Schafer JC, Goldenring JR, Taylor SS. D-AKAP2 interacts with Rab4 and Rab11 through its RGS domains and regulates transferrin receptor recycling. J Biol Chem. 2009; 284:32869–32880. [PubMed: 19797056]
52. Van Der Sluijs P, Hull M, Zahraoui A, Tavitian A, Goud B, Mellman I. The small GTP-binding protein rab4 is associated with early endosomes. Proc Natl Acad Sci U S A. 1991; 88:6313–6317. [PubMed: 1906178]
53. van der Sluijs P, Hull M, Webster P, Male P, Goud B, Mellman I. The small GTP-binding protein rab4 controls an early sorting event on the endocytic pathway. Cell. 1992; 70:729–740. [PubMed: 1516131]
54. Deneka M, Neeft M, Popa I, van Oort M, Sprong H, Oorschot V, Klumperman J, Schu P, van der Sluijs P. Rabaptin-5alpha/rabaptin-4 serves as a linker between rab4 and gamma(1)-adaptin in membrane recycling from endosomes. Embo J. 2003; 22:2645–2657. [PubMed: 12773381]
55. Ren M, Xu G, Zeng J, De Lemos-Chiarandini C, Adesnik M, Sabatini DD. Hydrolysis of GTP on rab11 is required for the direct delivery of transferrin from the pericentriolar recycling compartment to the cell surface but not from sorting endosomes. Proc Natl Acad Sci U S A. 1998; 95:6187–6192. [PubMed: 9600939]
56. Kouranti I, Sachse M, Arouche N, Goud B, Echard A. Rab35 regulates an endocytic recycling pathway essential for the terminal steps of cytokinesis. Curr Biol. 2006; 16:1719–1725. [PubMed: 16950109]
57. Allaire PD, Marat AL, Dall'Armi C, Di Paolo G, McPherson PS, Ritter B. The Connecdenn DENN domain: a GEF for Rab35 mediating cargo-specific exit from early endosomes. Mol Cell. 2010; 37:370–382. [PubMed: 20159556]
58. Hattula K, Furuhjelm J, Tikkanen J, Tanhuanpaa K, Laakkonen P, Peranen J. Characterization of the Rab8-specific membrane traffic route linked to protrusion formation. J Cell Sci. 2006; 119:4866–4877. [PubMed: 17105768]
59. Henry L, Sheff DR. Rab8 regulates basolateral secretory, but not recycling, traffic at the recycling endosome. Mol Biol Cell. 2008; 19:2059–2068. [PubMed: 18287531]
60. Magadan JG, Barbieri MA, Mesa R, Stahl PD, Mayorga LS. Rab22a regulates the sorting of transferrin to recycling endosomes. Mol Cell Biol. 2006; 26:2595–2614. [PubMed: 16537905]
61. Wolff NA, Lee WK, Abouhamed M, Thevenod F. Role of ARF6 in internalization of metal-binding proteins, metallothionein and transferrin, and cadmium-metallothionein toxicity in kidney proximal tubule cells. Toxicol Appl Pharmacol. 2008; 230:78–85. [PubMed: 18353411]
62. Klein S, Franco M, Chardin P, Luton F. Role of the Arf6 GDP/GTP cycle and Arf6 GTPase-activating proteins in actin remodeling and intracellular transport. J Biol Chem. 2006; 281:12352–12361. [PubMed: 16527809]

63. Montagnac G, de Forges H, Smythe E, Gueudry C, Romao M, Salamero J, Chavrier P. Decoupling of Activation and Effector Binding Underlies ARF6 Priming of Fast Endocytic Recycling. Curr Biol. 2011
64. Weigert R, Yeung AC, Li J, Donaldson JG. Rab22a regulates the recycling of membrane proteins internalized independently of clathrin. Mol Biol Cell. 2004; 15:3758–3770. [PubMed: 15181155]
65. Lin SX, Grant B, Hirsh D, Maxfield FR. Rme-1 regulates the distribution and function of the endocytic recycling compartment in mammalian cells. Nat Cell Biol. 2001; 3:567–572. [PubMed: 11389441]
66. Grant BD, Caplan S. Mechanisms of EHD/RME-1 protein function in endocytic transport. Traffic. 2008; 9:2043–2052. [PubMed: 18801062]
67. Rapaport D, Auerbach W, Naslavsky N, Pasmanik-Chor M, Galperin E, Fein A, Caplan S, Joyner AL, Horowitz M. Recycling to the plasma membrane is delayed in EHD1 knockout mice. Traffic. 2006; 7:52–60. [PubMed: 16445686]
68. Balklava Z, Pant S, Fares H, Grant BD. Genome-wide analysis identifies a general requirement for polarity proteins in endocytic traffic. Nat Cell Biol. 2007; 9:1066–1073. [PubMed: 17704769]
69. Pant S, Sharma M, Patel K, Caplan S, Carr CM, Grant BD. AMPH-1/Amphiphysin/Bin1 functions with RME-1/Ehd1 in endocytic recycling. Nat Cell Biol. 2009; 11:1399–1410. [PubMed: 19915558]
70. Traer CJ, Rutherford AC, Palmer KJ, Wassmer T, Oakley J, Attar N, Carlton JG, Kremerskothen J, Stephens DJ, Cullen PJ. SNX4 coordinates endosomal sorting of TfnR with dynein-mediated transport into the endocytic recycling compartment. Nat Cell Biol. 2007; 9:1370–1380. [PubMed: 17994011]
71. Iacopetta BJ, Morgan EH. The kinetics of transferrin endocytosis and iron uptake from transferrin in rabbit reticulocytes. The Journal of biological chemistry. 1983; 258:9108–9115. [PubMed: 6135697]
72. Klausner RD, Van Renswoude J, Ashwell G, Kempf C, Schechter AN, Dean A, Bridges KR. Receptor-mediated endocytosis of transferrin in K562 cells. J Biol Chem. 1983; 258:4715–4724. [PubMed: 6300098]
73. Kohno H, Tokunaga R. Transferrin and iron uptake by rat reticulocytes. J Biochem. 1985; 97:1181–1188. [PubMed: 2863261]
74. Wyllie JC. Transferrin uptake by rabbit alveolar macrophages in vitro. Br J Haematol. 1977; 37:17–24. [PubMed: 588476]
75. Karin M, Mintz B. Receptor-mediated endocytosis of transferrin in developmentally totipotent mouse teratocarcinoma stem cells. J Biol Chem. 1981; 256:3245–3252. [PubMed: 6259157]
76. Richardson D, Baker E. Two mechanisms of iron uptake from transferrin by melanoma cells. The effect of desferrioxamine and ferric ammonium citrate. J Biol Chem. 1992; 267:13972–13979. [PubMed: 1629195]
77. Slordahl S, Romslo I, Lamvik J. Binding of transferrin and uptake of iron by K-562 cells. Scand J Clin Lab Invest. 1984; 44:549–553. [PubMed: 6091257]
78. Young SP, Roberts S, Bomford A. Intracellular processing of transferrin and iron by isolated rat hepatocytes. Biochem J. 1985; 232:819–823. [PubMed: 4091824]
79. Vyoral D, Hradilek A, Neuwirt J. Transferrin and iron distribution in subcellular fractions of K562 cells in the early stages of transferrin endocytosis. Biochim Biophys Acta. 1992; 1137:148–154. [PubMed: 1420321]
80. Lamb JE, Ray F, Ward JH, Kushner JP, Kaplan J. Internalization and subcellular localization of transferrin and transferrin receptors in HeLa cells. J Biol Chem. 1983; 258:8751–8758. [PubMed: 6305999]
81. Hopkins CR, Trowbridge IS. Internalization and processing of transferrin and the transferrin receptor in human carcinoma A431 cells. J Cell Biol. 1983; 97:508–521. [PubMed: 6309862]
82. Aloj L, Lang L, Jagoda E, Neumann RD, Eckelman WC. Evaluation of human transferrin radiolabeled with N-succinimidyl 4-[fluorine-18](fluoromethyl) benzoate. J Nucl Med. 1996; 37:1408–1412. [PubMed: 8708785]

83. Jackle S, Runquist EA, Miranda-Brady S, Havel RJ. Trafficking of the epidermal growth factor receptor and transferrin in three hepatocytic endosomal fractions. J Biol Chem. 1991; 266:1396–1402. [PubMed: 1671034]
84. Dickson RB, Hanover JA, Willingham MC, Pastan I. Prelysosomal divergence of transferrin and epidermal growth factor during receptor-mediated endocytosis. Biochem. 1983; 22:5667–5674. [PubMed: 6317024]
85. Stein BS, Sussman HH. Demonstration of two distinct transferrin receptor recycling pathways and transferrin-independent receptor internalization in K562 cells. J Biol Chem. 1986; 261:10319–10331. [PubMed: 3015925]
86. Hemmaplardh D, Morgan EH. Transferrin uptake and release by reticulocytes treated with proteolytic enzymes and neuraminidase. Biochim Biophys Acta. 1976; 426:385–398. [PubMed: 1268204]
87. Sorokin LM, Morgan EH, Yeoh GC. Transferrin endocytosis and iron uptake in developing myogenic cells in culture: effects of microtubular and metabolic inhibitors, sulphydryl reagents and lysosomotrophic agents. J Cell Physiol. 1988; 137:483–489. [PubMed: 3192629]
88. Schmid SL, Carter LL. ATP is required for receptor-mediated endocytosis in intact cells. J Cell Biol. 1990; 111:2307–2318. [PubMed: 2126013]
89. Inoue T, Cavanaugh PG, Steck PA, Brunner N, Nicolson GL. Differences in transferrin response and numbers of transferrin receptors in rat and human mammary carcinoma lines of different metastatic potentials. J Cell Physiol. 1993; 156:212–217. [PubMed: 8314858]
90. Willander M, Al-Hilli S. Analysis of biomolecules using surface plasmons. Methods Mol Biol. 2009; 544:201–229. [PubMed: 19488702]
91. Schuck P. Use of surface plasmon resonance to probe the equilibrium and dynamic aspects of interactions between biological macromolecules. Annu Rev Biophys Biomol Struct. 1997; 26:541–566. [PubMed: 9241429]
92. Vaughn DE, Bjorkman PJ. High-affinity binding of the neonatal Fc receptor to its IgG ligand requires receptor immobilization. Biochem. 1997; 36:9374–9380. [PubMed: 9235980]
93. Lebron JA, Bennett MJ, Vaughn DE, Chirino AJ, Snow PM, Mintier GA, Feder JN, Bjorkman PJ. Crystal structure of the hemochromatosis protein HFE and characterization of its interaction with transferrin receptor. Cell. 1998; 93:111–123. [PubMed: 9546397]
94. West AP Jr, Bennett MJ, Sellers VM, Andrews NC, Enns CA, Bjorkman PJ. Comparison of the interactions of transferrin receptor and transferrin receptor 2 with transferrin and the hereditary hemochromatosis protein HFE. J Biol Chem. 2000; 275:38135–38138. [PubMed: 11027676]
95. Morton TA, Myszka DG. Kinetic analysis of macromolecular interactions using surface plasmon resonance biosensors. Methods Enzymol. 1998; 295:268–294. [PubMed: 9750223]
96. Wiley HS, Cunningham DD. A steady state model for analyzing the cellular binding, internalization and degradation of polypeptide ligands. Cell. 1981; 25:433–440. [PubMed: 6269748]
97. Schwartz AL, Fridovich SE, Lodish HF. Kinetics of internalization and recycling of the asialoglycoprotein receptor in a hepatoma cell line. J Biol Chem. 1982; 257:4230–4237. [PubMed: 6279629]
98. Ciechanover A, Schwartz AL, Dautry-Varsat A, Lodish HF. Kinetics of internalization and recycling of transferrin and the transferrin receptor in a human hepatoma cell line. Effect of lysosomotropic agents. J Biol Chem. 1983; 258:9681–9689. [PubMed: 6309781]
99. Davis RJ, Faucher M, Racaniello LK, Carruthers A, Czech MP. Insulin-like growth factor I and epidermal growth factor regulate the expression of transferrin receptors at the cell surface by distinct mechanisms. J Biol Chem. 1987; 262:13126–13134. [PubMed: 3498714]
100. Sainte-Marie J, Vidal M, Bette-Bobillo P, Philippot JR, Bienvenue A. The influence of transferrin binding to L2C guinea pig leukemic lymphocytes on the endocytosis cycle kinetics of its receptor. Eur J Biochem. 1991; 201:295–302. [PubMed: 1915375]
101. Watkins JA, Nunez MT, Gaete V, Alvarez O, Glass J. Kinetics of iron passage through subcellular compartments of rabbit reticulocytes. J Membr Biol. 1991; 119:141–149. [PubMed: 2046086]

102. Bomford A, Young SP, Williams R. Release of iron from the two iron-binding sites of transferrin by cultured human cells: modulation by methylamine. Biochem (Mosc). 1985; 24:3472–3478.
103. Girones N, Davis RJ. Comparison of the kinetics of cycling of the transferrin receptor in the presence or absence of bound diferric transferrin. Biochem J. 1989; 264:35–46. [PubMed: 2604716]
104. Lauffenburger, DA.; Linderman, JJ. Receptors: models for binding, trafficking, and signaling. Oxford University Press; New York; Oxford: 1993.
105. Weigel PH, Oka JA. Endocytosis and degradation mediated by the asialoglycoprotein receptor in isolated rat hepatocytes. J Biol Chem. 1982; 257:1201–1207. [PubMed: 6276377]
106. May WS, Tyler G. Phosphorylation of the surface transferrin receptor stimulates receptor internalization in HL60 leukemic cells. J Biol Chem. 1987; 262:16710–16718. [PubMed: 3479431]
107. van der Ende A, du Maine A, Schwartz AL, Strous GJ. Modulation of transferrin-receptor activity and recycling after induced differentiation of BeWo choriocarcinoma cells. J Biol Chem. 1990; 270:451–457.
108. Dautry-Varsat A, Ciechanover A, Lodish HF. pH and the recycling of transferrin during receptor-mediated endocytosis. Proc Natl Acad Sci U S A. 1983; 80:2258–2262. [PubMed: 6300903]
109. Shitara Y, Kato Y, Sugiyama Y. Effect of brefeldin A and lysosomotropic reagents on intracellular trafficking of epidermal growth factor and transferrin in Madin-Darby canine kidney epithelial cells. J Control Release. 1998; 55:35–43. [PubMed: 9795009]
110. Yazdi PT, Murphy RM. Quantitative analysis of protein synthesis inhibition by transferrin-toxin conjugates. Cancer Res. 1994; 54:6387–6394. [PubMed: 7987833]
111. Nunez MT, Glass J. The transferrin cycle and iron uptake in rabbit reticulocytes. Pulse studies using 59Fe, 125I-labeled transferrin. J Biol Chem. 1983; 258:9676–9680. [PubMed: 6885764]
112. Lao BJ, Tsai WL, Mashayekhi F, Pham EA, Mason AB, Kamei DT. Inhibition of transferrin iron release increases in vitro drug carrier efficacy. J Control Release. 2007; 117:403–412. [PubMed: 17239470]
113. Yoon DJ, Chu DS, Ng CW, Pham EA, Mason AB, Hudson DM, Smith VC, MacGillivray RT, Kamei DT. Genetically engineering transferrin to improve its in vitro ability to deliver cytotoxins. J Control Release. 2009; 133:178–184. [PubMed: 18992290]
114. Yoon DJ, Kwan BH, Chao FC, Nicolaides TP, Phillips JJ, Lam GY, Mason AB, Weiss WA, Kamei DT. Intratumoral therapy of glioblastoma multiforme using genetically engineered transferrin for drug delivery. Cancer Res. 2010; 70:4520–4527. [PubMed: 20460527]
115. Weaver M, Laske DW. Transferrin receptor ligand-targeted toxin conjugate (Tf-CRM107) for therapy of malignant gliomas. J Neurooncol. 2003; 65:3–13. [PubMed: 14649881]
116. Laske DW, Youle RJ, Oldfield EH. Tumor regression with regional distribution of the targeted toxin TF-CRM107 in patients with malignant brain tumors. Nat Med. 1997; 3:1362–1368. [PubMed: 9396606]
117. Debinski W. Molecular targeting with recombinant cytotoxins for the treatment of brain tumors. Drug Dev Res. 2008; 69:407–414.

Highlights

- We describe qualitative experiments using microscopy that have elucidated cellular components involved in transferrin internalization, sorting, and recycling.
- We examine quantitative experiments using radioactivity and surface plasmon resonance for Tf binding, internalization, recycling, and degradation.
- Quantitative experiments, combined with mathematical modeling, enable researchers to evaluate transferrin kinetic parameters and equilibrium dissociation constants.
- Mathematical models can be used to identify design parameters to improve the ability of transferrin to deliver anti-cancer agents.

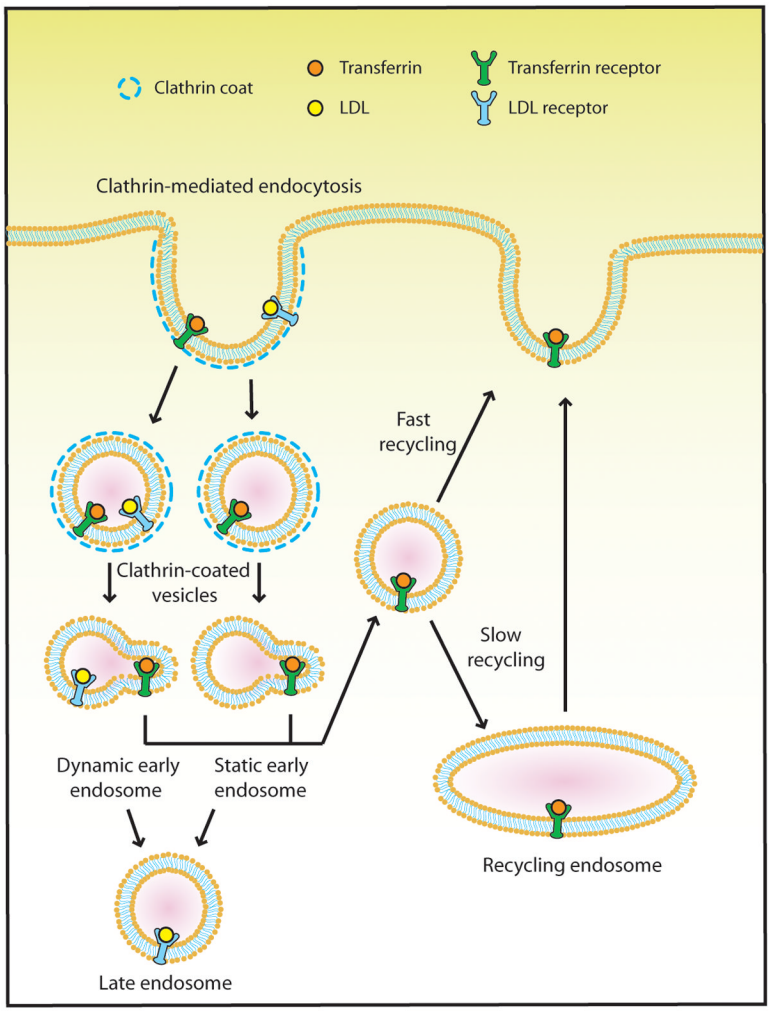

Figure 1. An overall diagram of Tf trafficking

Tf is internalized via clathrin-mediated endocytosis and taken up into clathrin-coated vesicles. After the uncoating of clathrin, Tf can be found in both populations of static and dynamic early endosomes, as Tf shows no preference for either population. LDL, which follows the degradation pathway, is trafficked preferentially to dynamic early endosomes. Tubulation occurs in both populations of early endosomes which proceeds to separate from early endosomes and traffic Tf to recycling pathways. A fast recycling route takes Tf directly back to the plasma membrane. A slower recycling route delivers Tf first to the perinuclear recycling compartment before Tf is trafficked back to the cell surface. For more information, a review by Conner and Schmid [13] and Grant and Donaldson [14] describes additional information in further detail on clathrin-mediated endocytosis and recycling pathways, respectively.

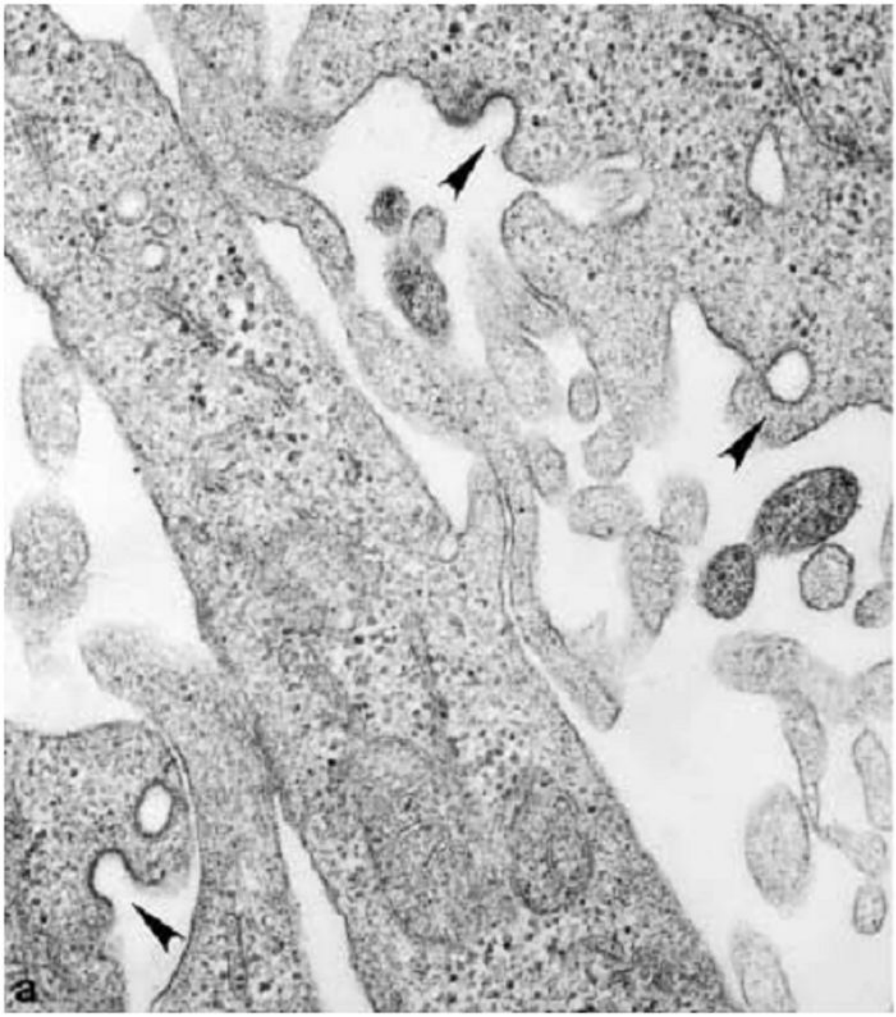

Figure 2. Clathrin-coated pits and vesicles formed during clathrin-mediated endocytosis of Tf

Electron microscopy can be used to visualize clathrin-coated pits and vesicles, as indicated by the collection of gold particle-TfR antibody conjugates within them. These collections are indicated by the black arrowheads. From Robinson and coworkers [27]. © The Rockefeller University Press. **The Journal of Cell Biology, 2003, 162: 909–918.**

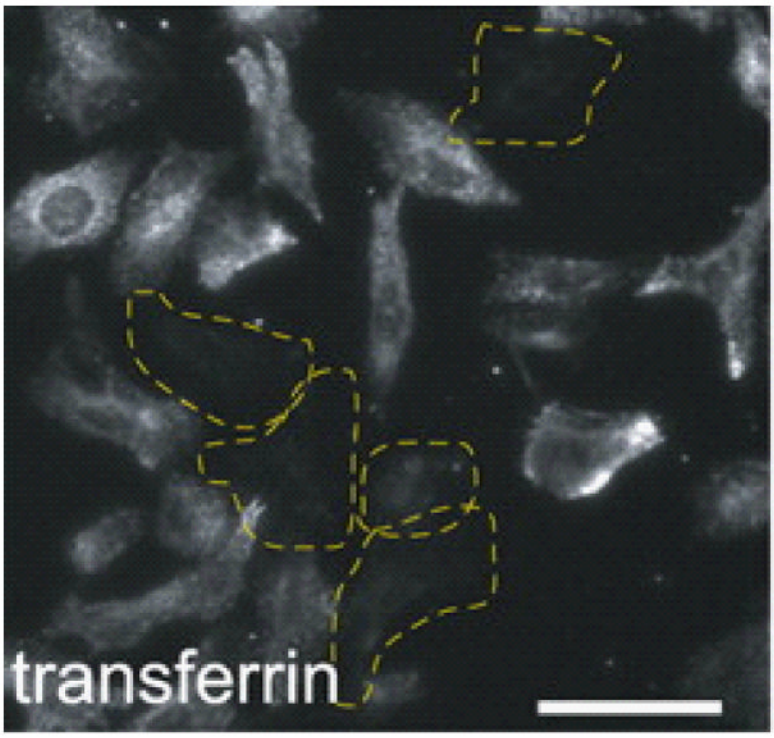

Figure 3. Laser-scanning confocal microscopy image of Tf internalization

Tf endocytosis is inhibited in cells experiencing PtdIns(4,5)P_2 reduction (outlined in yellow) as noted by their decreased levels of internalized fluorescent Tf. From Meyer and coworkers [33], reproduced/adapted with permission from the Journal of Cell Science.

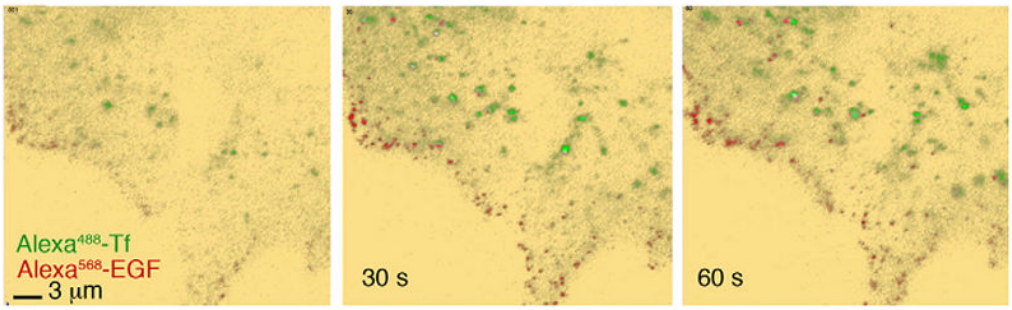

Figure 4. TIRF microscopy images of Tf (green) and EGF (red) within 60 seconds of addition to the cell

Both EGF and Tf separate into distinct groups while exhibiting minimal colocalization with each other. The researchers hypothesize that this early separation of ligands may be due to segregated regions of receptors in the plasma membrane that sort cargo prior to internalization. This figure from Corvera and coworkers [9] is reproduced/adapted with permission from the Journal of Cell Science.

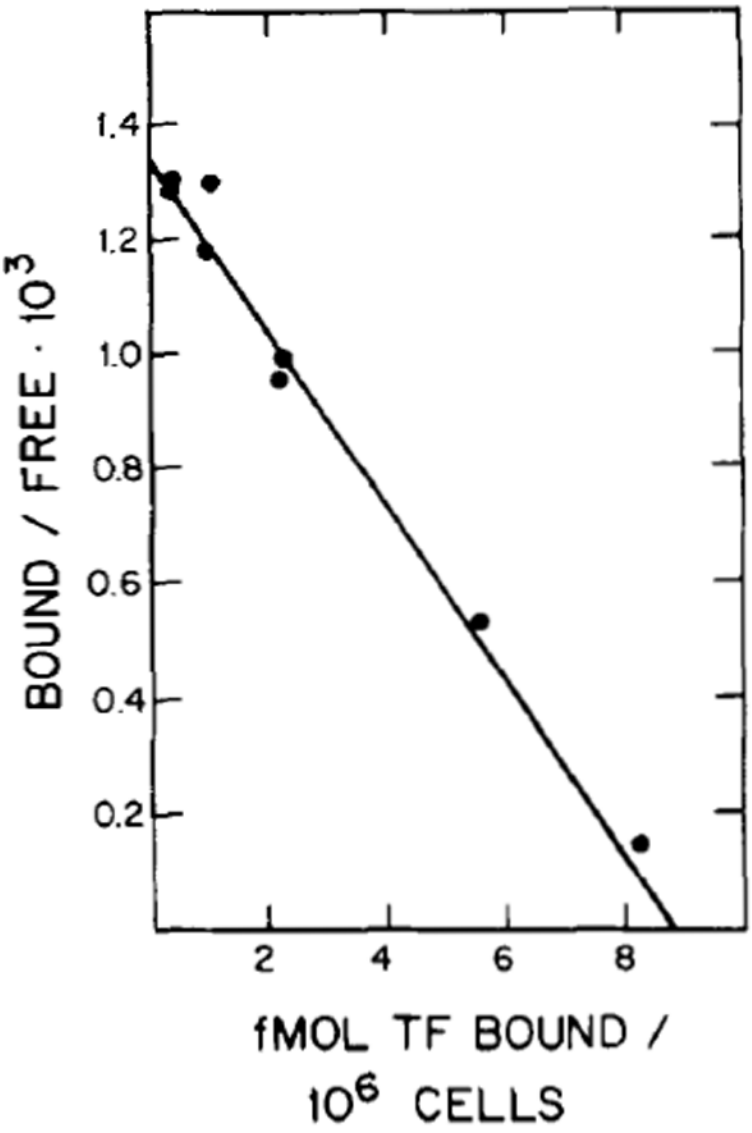

Figure 5. Scatchard plot of transferrin binding to mouse teratocarinoma stem cells

Bound, referred to as C_{eq} in text, is the equilibrium quantity of Tf bound to TfR at the cell surface in fmol Tf bound/10^6 cells, and *Free*, referred to as L_{eq} in text, is the concentration of free Tf present in the medium in μM. The equilibrium dissociation constant, K_D, can be found as the negative inverse of the slope in units of nM, and the total number of receptors per cell can be calculated from the y-intercept value. This research was originally published in the Journal of Biological Chemistry [75]. © The American Society for Biochemistry and Molecular Biology.

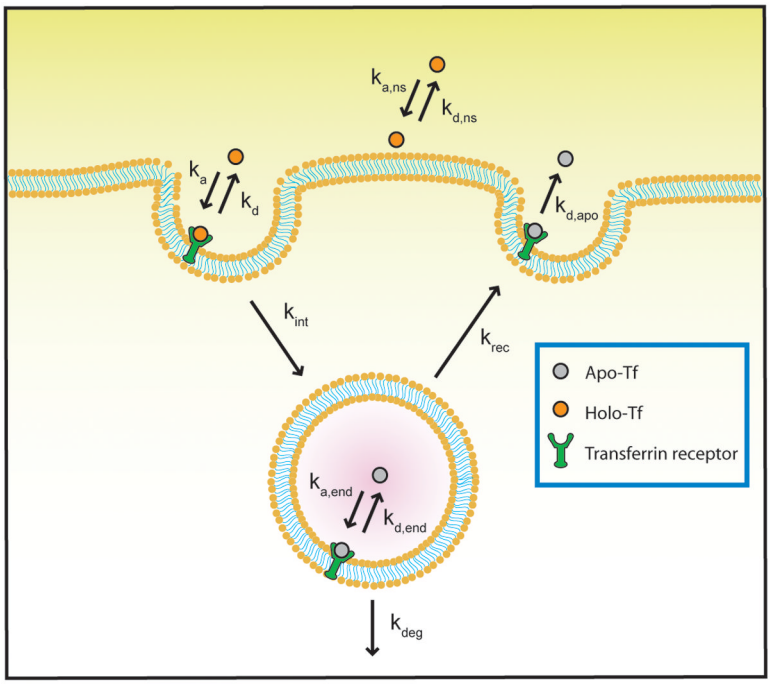

Figure 6. Illustration of kinetic rate constants for the Tf trafficking pathway

Holo-Tf binds to its receptor to initiate the pathway, which can be described by the association and dissociation constants, k_a and k_d. The Tf/TfR complex is then internalized with a rate constant of k_{int}. Once inside the endosome, iron is released forming apo-Tf, and the association and dissociation constants for binding inside the endosome, $k_{a,end}$ and $k_{d,end}$, can be evaluated. Subsequently, Tf can be transported to one of two pathways, degradation or recycling, which are described by k_{deg} and k_{rec}. However, apo-Tf typically is routed back to the cell surface via the recycling pathway. At the cell surface, apo-Tf is dissociated from TfR with a kinetic rate constant of $k_{d,apo}$. One model discussed also takes into consideration the nonspecific binding of Tf to the cell surface, which is described by $k_{a,ns}$ and $k_{d,ns}$.

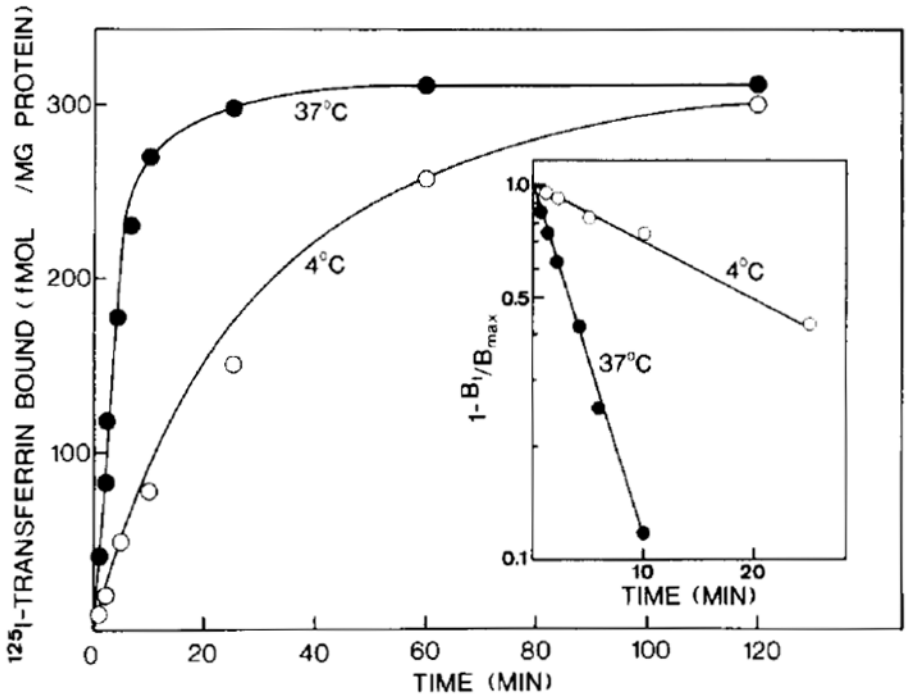

Figure 7. Rate of Tf binding to the cell surface

Radiolabeled Tf bound to the cell surface (fmol Tf/total mg protein) over time (min) was evaluated using low temperatures (4 °C) and energy inhibitors at physiological temperature. *Inset:* The semi-log plot of $(1-B_t/B_{max})$, where B_t is the amount of ligand bound at time t and B_{max} is the maximum amount of ligand bound, versus time allows for determination of the half-time of binding of Tf to the cell surface. Using the half-time, the rate constant for binding, k_a, can be determined. This research was originally published in the Journal of Biological Chemistry [98]. © The American Society for Biochemistry and Molecular Biology.

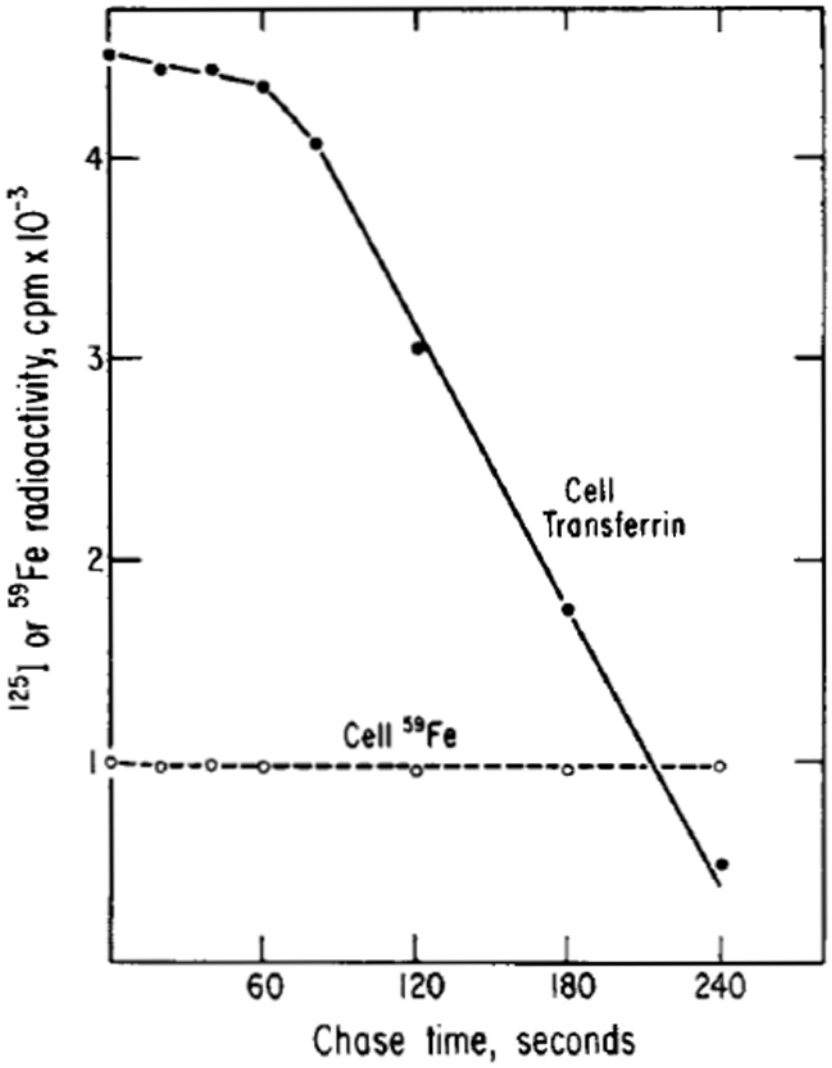

Figure 8. Kinetics of the Tf trafficking cycle

A 10 s pulse of ^{59}Fe-^{125}I-Tf was followed by a chase of excess unlabeled Tf. The total cell associated ^{59}Fe and ^{125}I-Tf were then measured at designated time points. Initially, a 60 s dwell period is observed in ^{125}I radioactivity, while the Tf is trafficked through the cell. Tf is then released from the cell with a half-time of 110 ± 14 s. In contrast, throughout the experiment, ^{59}Fe remains within the cell once delivered by Tf, as expected. The total cycle is completed within 260 ± 39 s. This research was originally published in the Journal of Biological Chemistry [111]. © The American Society for Biochemistry and Molecular Biology.

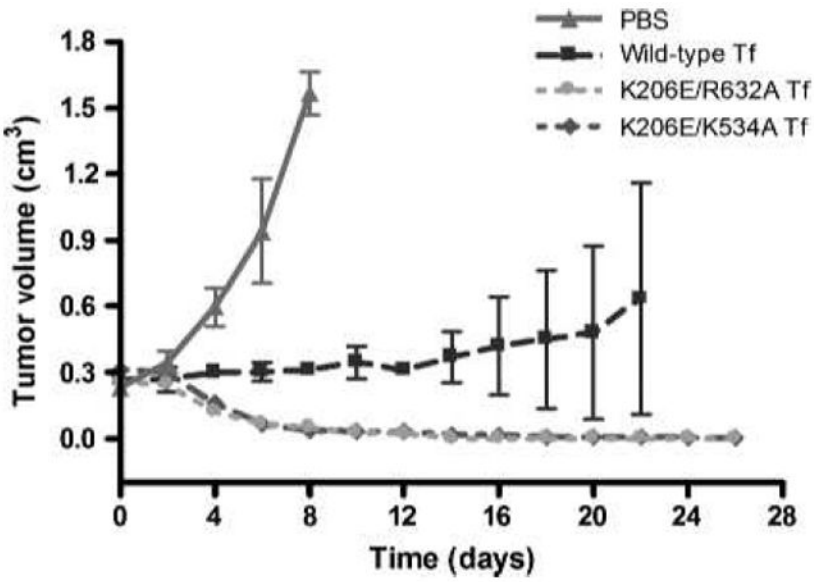

Figure 9. Regression of established flank tumors using mutant Tf conjugated to diphtheria toxin (DT)

A novel design criterion was determined using a mathematical model. When the iron release rate of Tf was reduced, an increased cellular association of the Tf mutants was observed. *In vivo* results showed nearly complete regression of tumor flank volume when female nude mice with established U87-derived glioma flank tumors were treated with the mutant Tf conjugated to DT, while wild-type Tf-DT conjugate only suppressed further tumor growth. From Kamei and coworkers [114]. Adapted and reprinted by permission from the American Association for Cancer Research: Yoon *et al*. Intratumoral therapy of glioblastoma multiforme using genetically engineered transferrin for drug delivery, Cancer Research, 2010, 70 (11), 4520–4527.

Table 1

Rate constants and cycling time of the transferrin trafficking pathway.

Rate Constants							Cycling Time	Cell Type	References
k_a (M^{-1} min^{-1})	k_d (min^{-1})	k_{int} (min^{-1})	$k_{end,a}$ (M^{-1} min^{-1})	$k_{end,d}$ (min^{-1})	k_{rec} (min^{-1})	k_{rel} (min^{-1})	T_c (min)		
		0.43 ± 0.07			0.48			isolated rabbit reticulocytes	[71]
$(9.6 \pm 0.24) \times 10^7$	0.078 ± 0.012		$(4.4 \pm 0.4) \times 10^7$	0.056 ± 0.012				N/A (SPR)	[93]
2.99×10^6	0.09	0.2			0.139	2.6	16.9	HepG2	[98]
2.7×10^7		0.33 ± 0.03			0.11	2.6		A431 Epidermoid Carcinoma cells	[99]
$(1.2 \pm 0.2) \times 10^6$	0.056 ± 0.01	0.214 ± 0.01			0.19 ± 0.03		14	guinea pig leukemic B lymphocytes	[100]
1.2×10^7		0.84					4.25 ± 0.72	isolated rabbit reticulocytes	[101]
		0.45			0.1			K562	[102]
		0.22 ± 0.02			0.065 ± 0.002			A431 Epidermoid Carcinoma cells	[103]
		0.183			0.113			HL60	[106]
		0.231			0.6		22.7	BeWo human choriocarcinoma cells	[107]
					0.02			Madin-Derby canine kidney epithelial cells	[109]
$(4 \pm 1) \times 10^7$	1.3 ± 0.5	0.38 ± 0.05			0.18 ± 0.02			HeLa	[110]
							4.33 ± 0.6	isolated rabbit reticulocytes	[111]